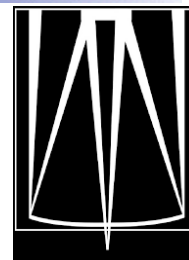




Simulated Performance of GNAO



GNAO-SYS-SIM-001

Related PBS ID: 5.2

M. van Dam, G. Sivo, E. Marin

April 13, 2020

Contents

1	Introduction	5
2	Simulation parameters	5
2.1	Atmospheric parameters	5
2.2	Dome seeing	5
2.3	Sodium return and Rayleigh	6
2.4	Laser launch telescope configuration	6
2.5	Optical throughput	7
2.6	LGS WFS camera	8
2.7	NGS WFS Camera	9
2.8	Windshake and vibrations	11
2.9	Deformable mirror characteristics	12
2.10	M2 print-through	12
2.11	Science metrics	13
3	Simulation description and results	13
3.1	Simulation tool	13
3.2	Rayleigh contamination	14
3.3	Constellations, guide star locations and Rayleigh backscatter	15
3.4	Interactuator spacing	23
3.5	DM conjugate altitude	24
3.6	DM characteristics	25
3.7	LGS detector selection	26
3.8	LGS WFS frame rate	26
3.9	Pixel angular extent and number of pixels	27
3.10	Dome seeing	28
3.11	Narrow-field performance	28
3.12	Science atmospheric dispersion corrector	29
4	NGS guide star performance	31
4.1	Limiting magnitude	31
4.2	Tip-tilt disturbances	32
4.3	Effect of atmospheric dispersion compensation	32
4.4	Sky coverage calculations	34
5	Semi-analytical calculations	37
5.1	High-order tomographic error	37
5.2	Classical fitting error	38
5.3	Generalized fitting error	39

6	Wavefront error budget	41
6.1	High-order wavefront errors.....	41
6.2	Tip-tilt errors	42
6.3	Focus errors	43
7	Conclusions.....	45
8	Appendix	45
8.1	LGS tomography	45
8.2	NGS tomography.....	45
8.3	Performance of 2 laser, 5 LGS system.....	47

Document Acceptance and Release Notice

This document is a managed document. To identify changes, each page contains a release number and a page number. This document is authorized for release once all signatures have been obtained.

APPROVED:	<i>Approval on file</i> _____ William Rambold GNAO Project Lead Systems Engineer	Date:	2020-11-12
APPROVED:	<i>Approval on file</i> _____ Manuel Lazo GNAO Project Manager	Date:	2020-11-12
APPROVED:	<i>Approval on file</i> _____ Gaetano Sivo GNAO Principal Investigator	Date:	2020-11-12
APPROVED:	<i>Approval on file</i> _____ Henry Roe GNAO Sponsor, Gemini Deputy Director	Date:	2020-11-12

Change Record

Version	Date	Description	Owner Name	Change Request
4.0	2020-11-12	Released through formal change control process	M. van Dam	GEM-186

1 Introduction

The Gemini North Adaptive Optics (GNAO) instrument is a next generation multi-conjugate adaptive optics (MCAO) system designed for a wide range of science cases. The aim is to produce near diffraction-limited image quality for J-, H- and K-bands. The requirement is for stable image quality across a 1' diameter field, with a K-band Strehl of between 0.3 (requirement) and 0.5 (goal). The system would use 2 deformable mirrors (DMs) at first light at conjugate altitudes of 0 km and 14 km. When an adaptive secondary mirror (ASM) is added, the DM conjugate to the ground can be moved to a conjugate altitude of 4 km. LGS-based AO systems require natural guide stars (NGSs) to measure tip-tilt and focus. GNAO has sky coverage requirements of 75% when using a single NGS, and 50% when using three NGSs.

This document presents simulation results in support of a preliminary design of GNAO. Parameter space is explored in order to see how the performance is impacted by the design.

2 Simulation parameters

In this section, we describe the list of inputs needed to run the simulations.

2.1 Atmospheric parameters

The atmospheric parameters are the 25th, 50th and 75th percentile sourced from the TMT (Table 1). The outer scale in every case is 30 m. Random wind directions were applied to the measured wind speeds. The design parameters will be optimized based on median seeing, and the performance evaluated for all three cases.

	Elevation (m)	0	500	1000	2000	4000	8000	16000
	Wind speed (m/s)	5.6	5.77	6.25	7.57	13.31	19.06	12.14
	Wind direction (°)	190	255	270	350	17	29	66
25%, $r_0 = 0.247$ m	Turbulence fraction	0.5152	0.0951	0.0322	0.0262	0.1160	0.0737	0.1416
50%, $r_0 = 0.186$ m		0.4557	0.1295	0.0442	0.0506	0.1167	0.0926	0.1107
75%, $r_0 = 0.135$ m		0.3952	0.1665	0.0703	0.0773	0.0995	0.1069	0.0843

Table 1: Turbulence profile used for Mauna Kea 25th, 50th and 75th percentiles with r_0 quoted at a wavelength of 500 nm.

The system must operate down to a zenith angle of 50°.

2.2 Dome seeing

The dome seeing at Gemini North is believed to be very benign, with a dome seeing FWHM of 0.13" at 500 nm. Most simulations were run without including dome seeing. The simulations with the dome seeing used a C_n^2 value of $2.28e-14$, which is 10% of the total turbulence.

2.3 Sodium return and Rayleigh

Holzlohner and predicts a return of $14 \text{ Mph m}^{-2}\text{s}^{-1}$ at the optimal pointing direction with a 20 W TOPTICA laser of which 16 W are launched at the Maunakea site with atmospheric transmission of 0.84.¹ The sodium density for this calculation is $3.75 \times 10^{13} \text{ atoms m}^{-2}$.

For Keck II, with a collecting area of 76 m^2 , and a 22 W laser, the expected return at the optimal pointing direction is 1.17×10^9 . Using the Keck II telescope, the measured return at zenith using a 22 W laser corresponds to the same subaperture intensity in the WFS as an $m_R = 7.5 \pm 0.2 \text{ star}$.² Using a photometric zero point of $1.49 \times 10^{12} \text{ photons per second}$ at the top of the telescope for VR-band, this gives $1.48 \times 10^9 \text{ photons/second}$ for the telescope, so it is consistent with the expected return.

For Gemini, the collecting area is 48 m^2 . Holzlohner predicts a value of $6.72 \times 10^8 \text{ photons/sec}$ for the whole telescope using a 20 W laser. I assumed a value of 3.10×10^8 at the top of the telescope, which is conservative. The reason for this is that other pointing directions can have a factor of two reduction in return, while the sodium density can also vary by a factor of two or more.

Recall that in most cases, the laser light is divided into two before propagating. This is modeled by assuming that each beam is 10 W.

In the simulations, we assume that the subapertures contaminated by Rayleigh backscatter will be masked and unused, which is the way that GeMS operates.

2.4 Laser launch telescope configuration

Three configurations of lasers and launch telescopes are under consideration, as shown in Figure 1. For Configuration 1, a single laser is launched from behind the secondary, while two lasers are split into two beams each. For Configuration 2, three lasers are split into six beams, while Configuration 3 has two lasers split into four beams.

¹Holzlohner R. et al., "Optimization of CW Sodium Laser Guide Star Efficiency," A&A 510, 0004-6361 January, (2016).

²Chin, Jason CY, et al. "Keck II laser guide star AO system and performance with the TOPTICA/MPBC laser." Adaptive Optics Systems V. Vol. 9909. International Society for Optics and Photonics, 2016.

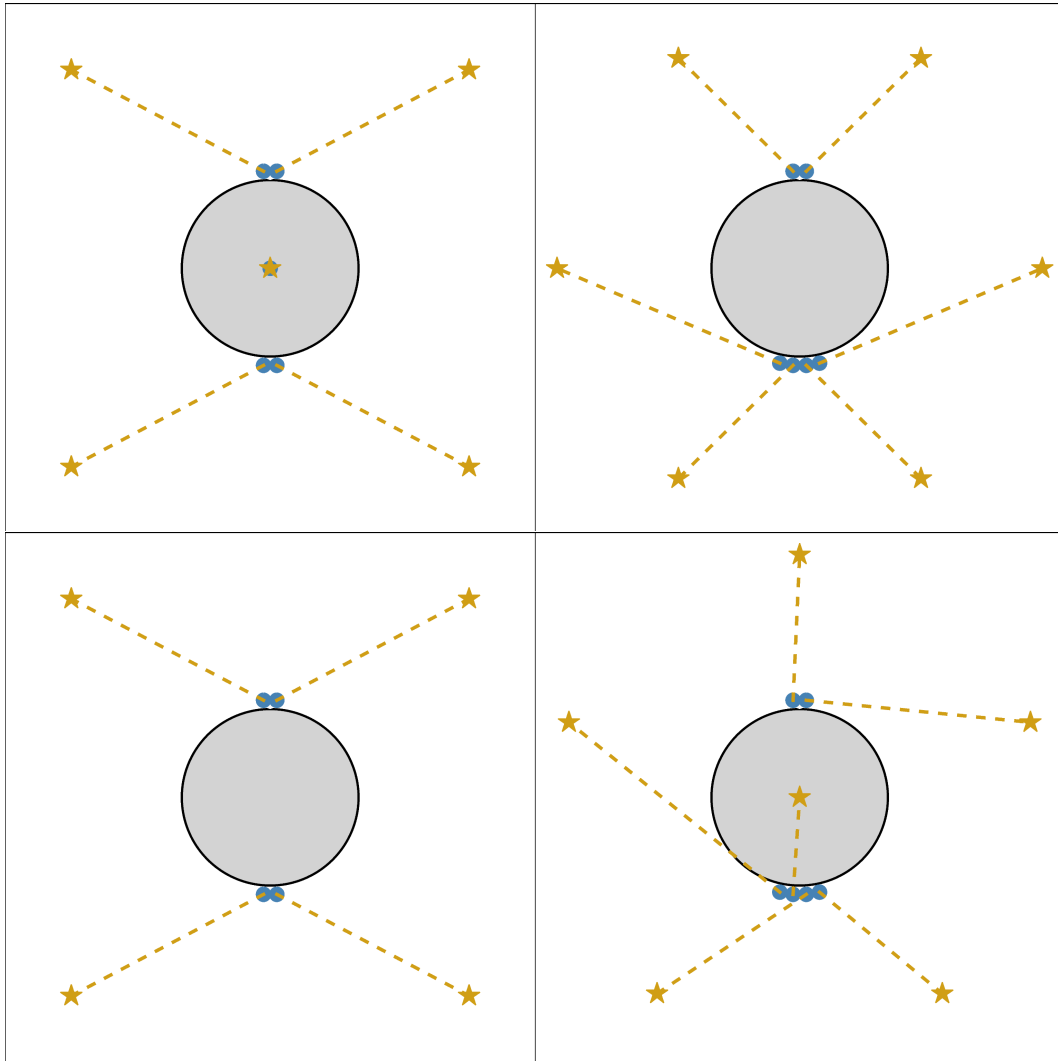


Figure 1: Configurations 1 (top left), 2 (top right), 3 (bottom left) and 4 (bottom right). Note that 1, 2 and 4 use 3 LGSs, while 3 uses 2 LGSs.

2.5 Optical throughput

The optical throughput of the atmosphere is 0.89, the telescope is 0.821, and GNAO is 0.3, for a total of 0.22. The breakdown in optical throughput was provided by Emmanuel Chirre and is reproduced in Table 2.

Optic	Refl or Trans	I	J	H	K
		0.85	1.25	1.65	2.2
OAP1	R	0.973	0.973	0.973	0.973
DM14	R	0.99	0.99	0.99	0.99
TTM	R	0.98	0.98	0.98	0.98
NIR ADC	T	0.6	0.61	0.58	0.396
OAP2	R	0.973	0.973	0.973	0.973
M1	R	0.99	0.99	0.99	0.99
M2	R	0.99	0.99	0.99	0.99
OAP3	R	0.973	0.973	0.973	0.973
DM4	R	0.99	0.99	0.99	0.99
DM0	R	0.99	0.99	0.99	0.99
SC BS	T	0.933	0.9337	0.935	0.936
M3	R	0.99	0.99	0.99	0.99
OAP4	R	0.973	0.973	0.973	0.973
TOTAL		0.46	0.47	0.45	0.31

Table 2: Throughput of reflective and transmissive GNAO optics.

2.6 LGS WFS camera

The baseline detector is an OCAM2 camera, which is based on the CCD220, a 240x240 pixel detector. This is CCD uses electron multiplication, which allows us to get subelectron read noise. The penalty to be paid is the increase in the excess noise factor from 1 to 1.41, which is equivalent to reducing the quantum efficiency of the detector by a factor of 2. The best wavefront sensing CCD on the market (to our knowledge) is the Lincoln Labs CCID75, which has better than 3 e- read noise. CMOS cameras currently on the market will not be considered as they have not yet transitioned into astronomical AO. The properties of the two candidate wavefront sensing cameras are tabulated in Table 3. The read noise of OCAM2 can be reduced by increasing the multiplication gain, but this ages the camera faster and should be avoided.

Camera	OCAM2	CCID75
Pixels	240x240	160x160
Excess noise	1.41	1
Quantum efficiency @589 nm	0.90	0.90
Read noise	0.5 e-	2 e-
Dark current	10 e-/s	48 e-/s
Charge diffusion FWHM	0.5 pixels (?)	0.25 pixels

Table 3: Properties of wavefront sensing cameras. The OCAM2 properties were obtained from Feautrier *et al.*,³ while the CCID82 properties were extracted from Baranec *et al.*⁴ The question marks indicate educated guesses.

2.7 NGS WFS Camera

An NGS is needed to measure tip-tilt across the field, focus and (ideally) LGS aberrations.⁵ The tip-tilt and tip-tilt a measurement is made at a frame rate of 100 Hz or more using (ideally) three tip-tilt stars, while the focus measurement can be made at a much slower rate (at least one measurement per minute). The focus and truth sensor has not yet been defined. Three options are being considered for the pick-off, which affect the throughput to the NGS sensor. A beamsplitter that splits light across the full field between the two sensors, a pick-off mirror that sends all the light from one star to the truth sensor, and a pick-off dichroic that sends part of the light from the brightest star to the truth sensor. We will assume that 90% of the light across the full field is sent to the tip-tilt sensor, so the total throughput is $0.22 \times 0.90 = 0.20$.

The tip-tilt sensing camera mirrors the NGS2 tip-tilt sensor to be inserted on Canopus in July 2019. The noise characteristics are tabulated in Table 4. The read noise is 300 / EM gain. The read noise can be reduced to less than 0.1 e- using a higher electron multiplication gain, which stresses and ages the camera. There is an additional limitation in the NGS2 sensor: the full well is 800 kiloelectrons / EM gain. The EM gain needs to be set so that the brightest star does not saturate, which will not be optimal for the faintest stars. We ignore this limitation in this report, and note that there are other alternative cameras, such as the C-MORE camera from First Light Imaging.

³Feautrier, Philippe, et al. "Characterization of OCam and CCD220: the fastest and most sensitive camera to date for AO wavefront sensing." Adaptive Optics Systems II. Vol. 7736. International Society for Optics and Photonics, 2010.

⁴Baranec, Christoph, et al. "Second generation Robo-AO instruments and systems." Adaptive Optics Systems IV. Vol. 9148. International Society for Optics and Photonics, 2014.

⁵Clare, Richard M., Marcos A. van Dam, and Antonin H. Bouchez. "Modeling low order aberrations in laser guide star adaptive optics systems." Optics express 15.8 (2007): 4711-4725.

Camera	CCD
Pixels	512x512
Maximum frame rate ⁶	800 Hz
Excess noise	1.41
Quantum efficiency VRI-bands ⁷	0.80
Read noise	0.5 e-
Dark current ⁶	0.00058 e-/s
Charge diffusion FWHM	0.25 pixels

Table 4: Properties of the NGS2 wavefront sensing camera.

The quantum efficiency as a function of wavelength is plotted in Figure 2. If we pass the same wavelength range as NGS2 (450-950 nm), the photometric parameters are presented in Table 5.

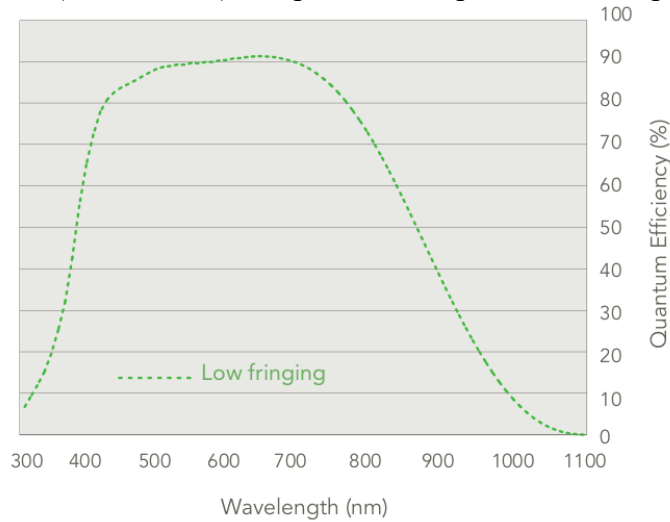


Figure 2: Quantum efficiency as a function of wavelength for the Nuvu Nnu512 IS camera.

Parameter	Value
Passband	450 - 950 nm
Photometric zero point (photons / second)	1.30e12
Sky background (magnitude / arcsec ²)	18.5

Table 5: Photometric parameters used in the simulations.

The NGS2 system for GeMS allows only a single frame rate to be used for all ROIs. Correia *et al* found no benefit to running some tip-tilt sensors faster than others for MCAO.⁸ However, intuitively it would seem that having one tip-tilt sensor running faster should reduce the effect of vibration. We defer consideration of a multi-frame rate system until later.

⁶Rigaut, François, et al. "NGS2: a focal plane array upgrade for the GeMS multiple tip-tilt wavefront sensor." *Adaptive Optics Systems V*. Vol. 9909. International Society for Optics and Photonics, 2016.

⁷http://www.nuvucameras.com/wp-content/uploads/2018/02/NuvuCameras-HNu512_IS.pdf

⁸Correia, Carlos, et al. "Increased sky coverage with optimal correction of tilt and tilt-anisoplanatism modes in laser-guide-star multiconjugate adaptive optics." *JOSA A* 30.4 (2013): 604-615.

2.8 Windshake and vibrations

It is well-known that there are strong vibrations at Gemini North, which have been described elsewhere.^{9,10}In this study, we add the tip-tilt disturbance measured by Altair at 1 kHz. The power spectral density corresponding to these disturbances are plotted in Figure 3. The YAO simulations already include the atmospheric tip-tilt, but it is not possible to distinguish and remove the atmospheric contribution from the telescope contribution.

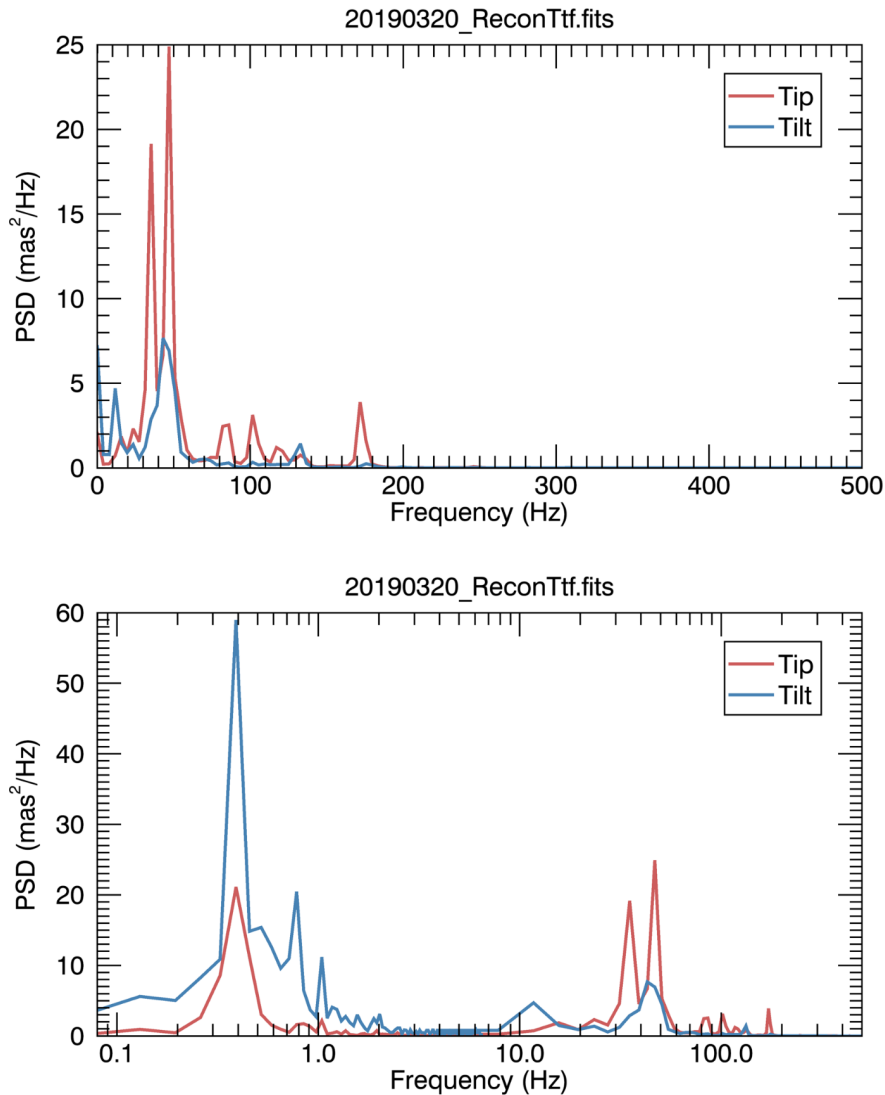


Figure 3: Power spectral density of the tip-tilt disturbance measured by Altair, plotted on a linear scale (top) and logarithmic scale (bottom).

The yao simulations use a time series for tip-tilt, and these were extracted directly from the Altair circular buffers. The buffer 20190320_ReconTtf.fits was used as it was representative of the 14 files provided. The main point to note is that there is a lot of energy over 30 Hz, which are frequencies that are not well corrected by the control loop if running at 1000 Hz or less.

⁹Christou, Julian C., et al. "ALTAIR performance and updates at Gemini North." Adaptive Optics Systems II. Vol. 7736. International Society for Optics and Photonics, 2010.

¹⁰Lai, Olivier, et al. "Altair performance and upgrades." Adaptive Optics Systems IV. Vol. 9148. International Society for Optics and Photonics, 2014.

2.9 Deformable mirror characteristics

GNAO will have two DMs, one conjugate to the ground, and the other conjugate to 14 km. If an adaptive secondary mirror (ASM) is implemented, the first DM will be moved to a conjugate altitude of 4 km. The vendor for the deformable mirrors (DMs) has not been selected, so a generic DM with a grid of actuators is used in the simulations with properties described in Table 6.

Property	Value
DM coupling	0.15
Hysteresis	0
Stroke	Unlimited
Bad actuators	0

Table 6: Properties of the DM used in the simulations.

The DM coupling can affect the ability to generate high spatial frequencies, but this is not an issue for commonly used DMs (e.g., Xinetics and CILAS). It has been shown that DM hysteresis does not affect the performance of a closed-loop MCAO system. The most important parameter from the point of view of operations is the stroke. GeMS is severely limited in stroke, which affects the performance in moderate to bad seeing, while the stroke limitation also leads to an increase in the time it takes to acquire a target, since we must wait for an offload of the low-order modes of the DM to the telescope. Specification of a minimum stroke requires knowledge of the atmosphere but also the optical aberrations in the common path of the AO system as well as in the science path.

2.10 M2 print-through

The secondary mirror at Gemini North has a well-known print-through error. The effect that this has on AO performance was investigated by Lai et al.¹¹ They measured the wavefront error due to the print-through and deduced from simulations what the effect this has on the image quality delivered by the AO system. The reduction in Strehl ratio on the science path, due to WFS aliasing, and due to a combination of both is reproduced in Table 7.

	WFS	Science path	Common
J-band	0.68	0.92	0.65
H-band	0.76	0.92	0.73
K-band	0.83	0.93	0.79

Table 7: Reduction in Strehl ratio due to M2 print-through if the wavefront aberration is only sensed by the WFS, only sensed by the science detector or sensed by both.¹¹

The wavefront error due to the print-through is plotted in Figure 4. Unfortunately, the magnitude of the print-through is unknown. We will assume that the value on the right hand column represents the reduction in Strehl ratio for GNAO, unless the existing secondary mirror is replaced by the spare (which needs to be repolished) or by an adaptive secondary mirror.

¹¹Lai, Olivier, et al. "Altair performance and upgrades." Adaptive Optics Systems IV. Vol. 9148. International Society for Optics and Photonics, 2014.

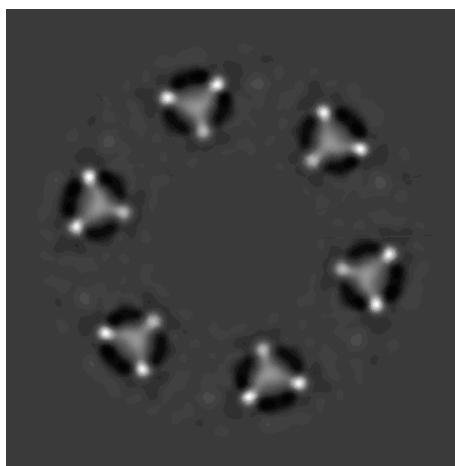


Figure 4: Wavefront error due to print-through

2.11 Science metrics

The image quality metrics calculated by default are the Strehl ratio, the Full Width at Half Maximum (FWHM), and the 50% encircled energy diameter. Other image quality metrics can also be computed if desired. The wavelengths of interest are 1.25, 1.65, 2.2, 3.55 and 4.77 microns, which corresponds approximately to the central wavelengths of J-, H-, K-, L- and M-bands. The target locations are in a regular grid with positions $[-47.4'', -31.6'', -15.8'', 0'', 15.8'', 31.6'', 47.4'']$ in both x and y, over a circle with a diameter of $2'$, as shown in Figure 5.

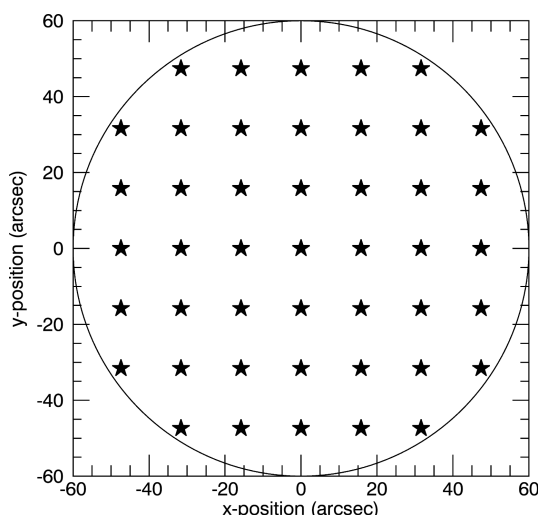


Figure 5: Location of science targets used to optimize the wavefront correction and to evaluate the image quality delivered by GNAO.

3 Simulation description and results

3.1 Simulation tool

End-to-end Monte-Carlo simulations were run using YAO,¹²⁻¹³ an open-source, user-configurable code written in the yorick language, along with custom scripts and parameter files. This code has over 100 users and has been used extensively to design and operate GeMS, the Gemini South MCAO system.

Some modifications to the YAO code base were made to support specific features needed for this

¹²Rigaut, François, and Marcos van Dam. "Simulating astronomical adaptive optics systems using Yao." AO4ELT (2013).

¹³<http://frigaut.github.io/yao/>

work, and these changes have been released for general use. In particular, Rayleigh contamination from off-axis launch locations had not been implemented (Section 14). Also, valid subaperture selection based on the ratio between the Rayleigh backscatter and the sodium return was missing, and this is now included.

The control law used in the simulations is very simple. The high-order loop uses a leaky integrator with a loop gain of 0.4 and a leak of 0.01. The tip-tilt loop also has a gain of 0.4, while the up-link tip-tilt loop has a gain of 0.1. A more sophisticated approach is needed to improve the tip-tilt performance, but the implementation of such a controller is beyond the scope of this report. In all cases, the loop delay was one frame.

Tomographic wavefront reconstructors for MCAO are not fully implemented in YAO. The wavefront reconstructors are hand-coded using a custom yorick script. A description of the high-order wavefront tomographic reconstructor is presented in Section 45, while the tip-tilt tomographic reconstructor is described in 45.

3.2 Rayleigh contamination

We are interested in knowing the impact of Rayleigh contamination (called fratricide) on the three laser configurations. Rayleigh contamination was only supported in yao for on-axis laser launch telescopes, and the functionality was extended to include laser launch telescopes at arbitrary locations. The modifications to the code were tested against the Rayleigh contamination simulated for the Giant Magellan Telescope (six LGSs using launch telescopes at three locations). Visual inspection of the Rayleigh pattern agreed with what was presented in Figure 5 of Conan et al.¹⁴ The Rayleigh for the three configurations is plotted in Figure 6. The fratricide is greatest for Configuration 1 due to the center launch of one laser, while Configuration 3 has essentially no fratricide. The impact of fratricide on AO performance is investigated in Section 15.

¹⁴Conan, Rodolphe, et al. "The Giant Magellan Telescope laser tomography adaptive optics system." *Adaptive Optics Systems III*. Vol. 8447. International Society for Optics and Photonics, 2012.

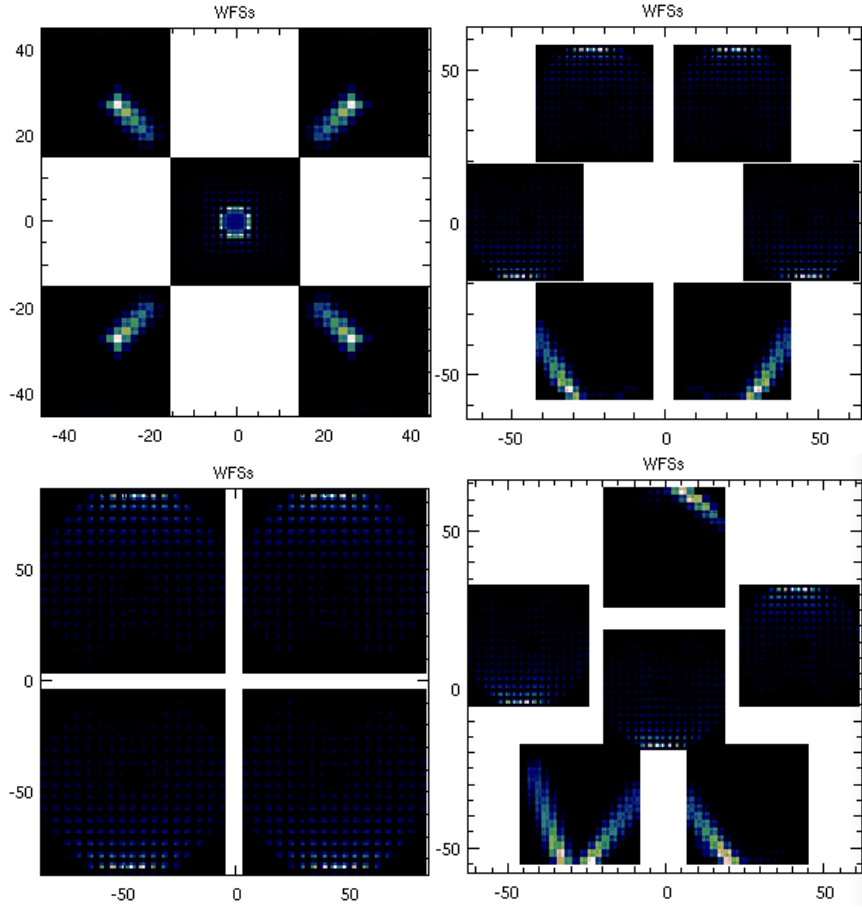


Figure 6: Screenshot of YAO simulation indicating the Rayleigh contamination for Configurations 1, 2, 3 and 4. The Rayleigh contamination for Configuration 3 is negligible.

3.3 Constellations, guide star locations and Rayleigh backscatter

In this section, we evaluate the performance for the three constellations using different guide star radii. We also evaluate the impact of Rayleigh backscatter on AO performance.

The parameters used in the simulations are as follows:

- 16x16 SH WFS with 4x4 1" pixels
- the interactor spacing of the DMs is the same as the pitch of the subapertures (~50 cm), with one DM at 0 km, the other at 14 km.
- three ideal tip-tilt sensing measurements to correct tip-tilt and the plate scale modes
- tip-tilt guide star locations are [0", +35"], [+40", -30"] and [-40", -20"]
- simulations were run at zenith and at 45° zenith angle
- median atmospheric conditions
- science field of view is a 2' diameter
- with and without Rayleigh backscatter (fratricide)

The average K-band Strehl ratio from the simulations is plotted in Figure 7, in conjunction to the standard deviation across the 2' diameter field. The results show that there is a soft dependence on radial distance, with the optimal average Strehl found for an LGS radial distance of 50" for Configuration 1, which also has an LGS at the center, and about 40" for the Configurations 2 and 3, which do not have the additional LGS. The variation in Strehl, however, decreases with increasing radial distance.

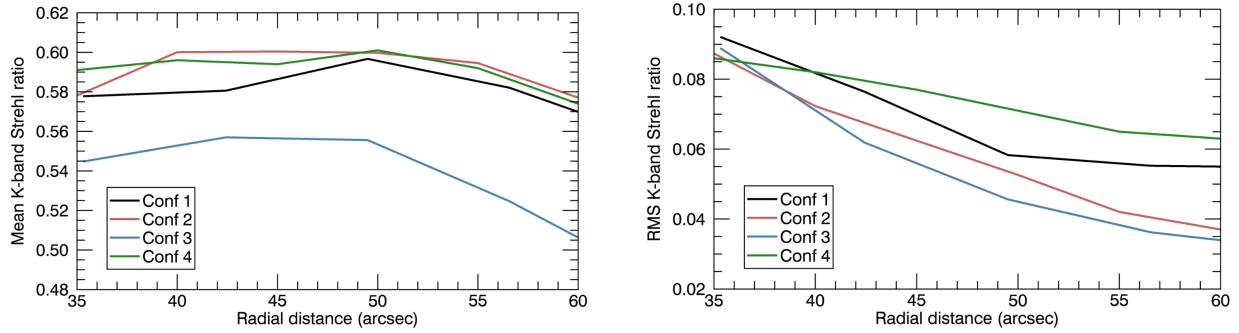


Figure 7: Simulated K-band Strehl ratio average and variation across the field for the three different configurations in median seeing. The radial distance is the distance of the off-axis laser guide stars from the optical axis. The simulations were run at zenith.

The fratricide has only a small effect on the results for Configurations 1 and 2, and no effect at all for Configuration 3, as expected. The results with and without fratricide for the three configurations are tabulated in Tables 8, 10 and 9. Note that the effect of fratricide increases with increasing guide star radial distance because there is less redundancy in the WFS measurements.

Guide star locations [$\pm x, \pm x$]	25''	30''	35''	40''	45''
With fratricide	0.578 \pm 0.092	0.581 \pm 0.076	0.597 \pm 0.058	0.582 \pm 0.055	0.557 \pm 0.055
No fratricide	0.580 \pm 0.090	0.583 \pm 0.076	0.604 \pm 0.061	0.595 \pm 0.054	0.568 \pm 0.051

Table 8: K-band Strehl ratio (average and standard deviation across the field) for Configuration 1, with and without fratricide.

Guide star dist	35''	40''	45''	50''	55''	60''
With fratricide	0.578 \pm 0.087	0.600 \pm 0.072	0.600 \pm 0.062	0.600 \pm 0.052	0.595 \pm 0.042	0.577 \pm 0.037
No fratricide	0.597 \pm 0.085	0.619 \pm 0.070	0.625 \pm 0.059	0.622 \pm 0.050	0.601 \pm 0.041	0.586 \pm 0.038

Table 9: K-band Strehl ratio (average and standard deviation across the field) for Configuration 2, with and without fratricide.

Guide star locations [$\pm x, \pm x$]	25''	30''	35''	40''	45''
With fratricide	0.545 \pm 0.557	0.557 \pm 0.062	0.556 \pm 0.046	0.525 \pm 0.036	0.487 \pm 0.032
No fratricide	0.546 \pm 0.089	0.558 \pm 0.062	0.558 \pm 0.046	0.525 \pm 0.036	0.487 \pm 0.032

Table 10: K-band Strehl ratio (average and standard deviation across the field) for Configuration 3, with and without fratricide.

Guide star dist	35''	40''	45''	50''	55''	60''
With fratricide	0.591 \pm 0.086	0.596 \pm 0.082	0.594 \pm 0.077	0.601 \pm 0.071	0.592 \pm 0.065	0.574 \pm 0.063
No fratricide	0.598 \pm 0.084	0.603 \pm 0.081	0.603 \pm 0.076	0.610 \pm 0.070	0.602 \pm 0.065	0.586 \pm 0.063

Table 11: K-band Strehl ratio (average and standard deviation across the field) for Configuration 4, with and without fratricide.

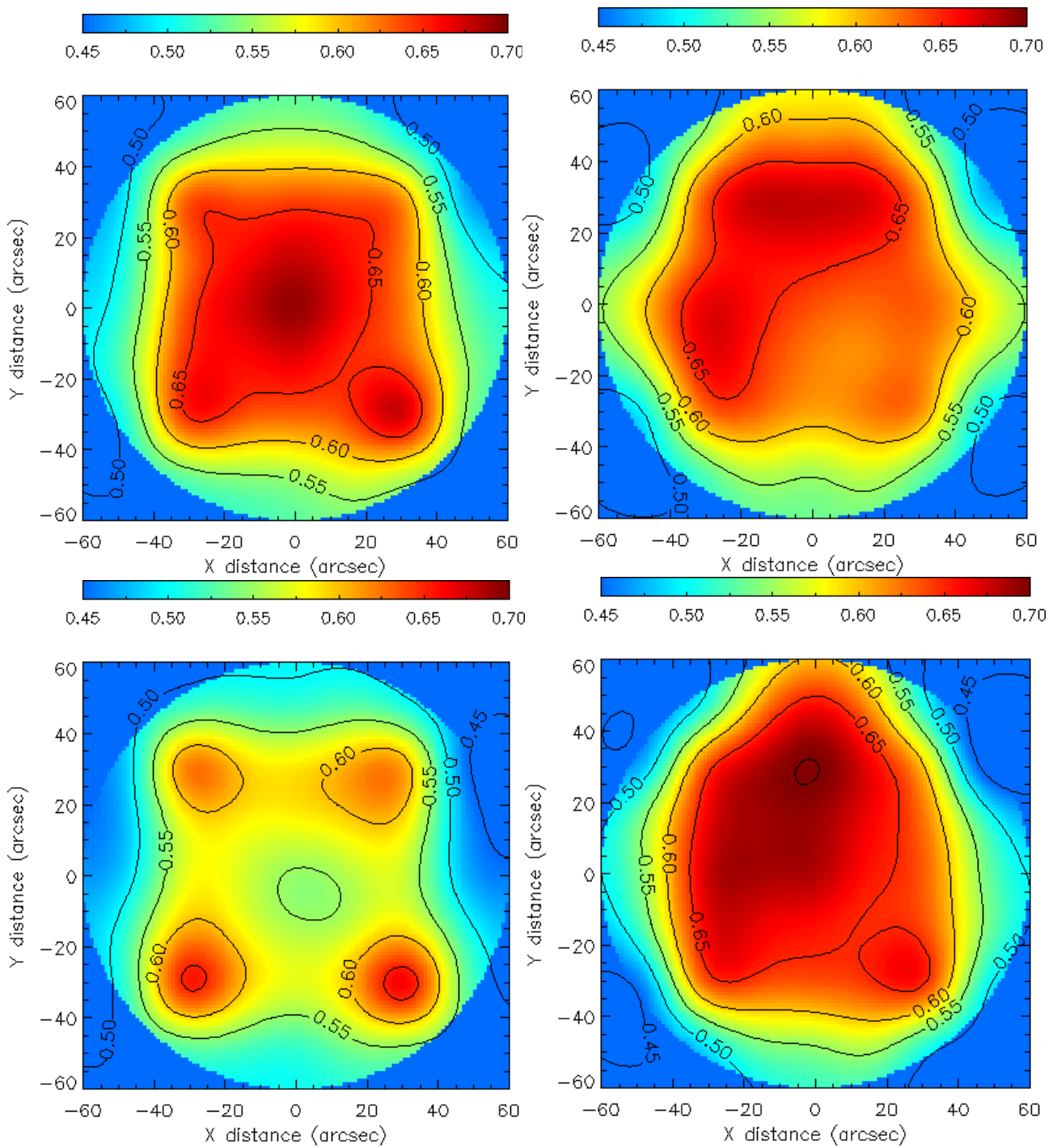


Figure 8: Variation in K-band Strehl ratio across the field at zenith for Configurations 1, 2, 3 and 4. The radial distance in all cases was 50".

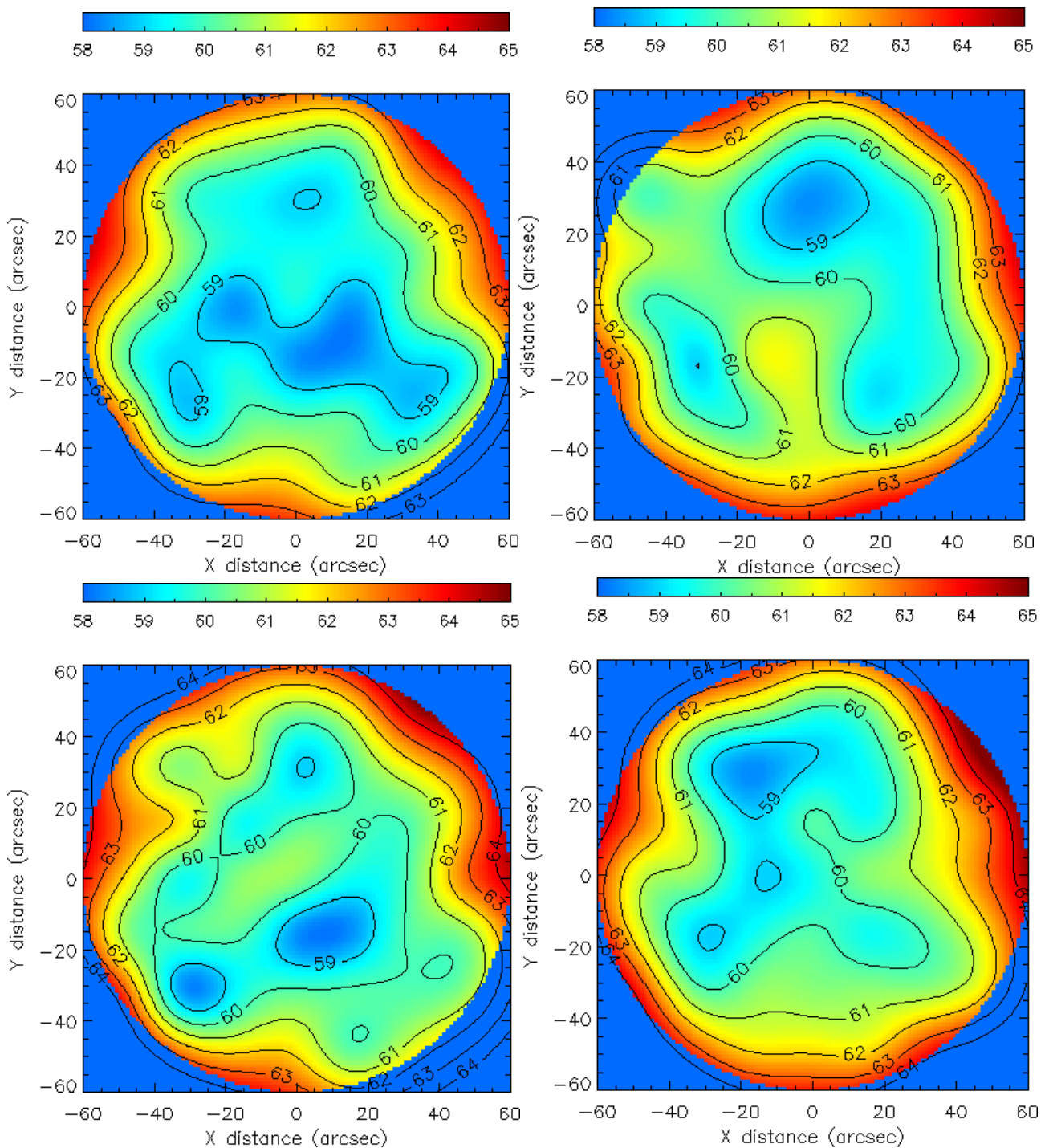


Figure 9: Variation in K-band FWHM across the field at zenith for Configurations 1, 2, 3 and 4. The radial distance in all cases was 50".

Grids of PSFs were generated for all of the configurations and are plotted in Figure 10.

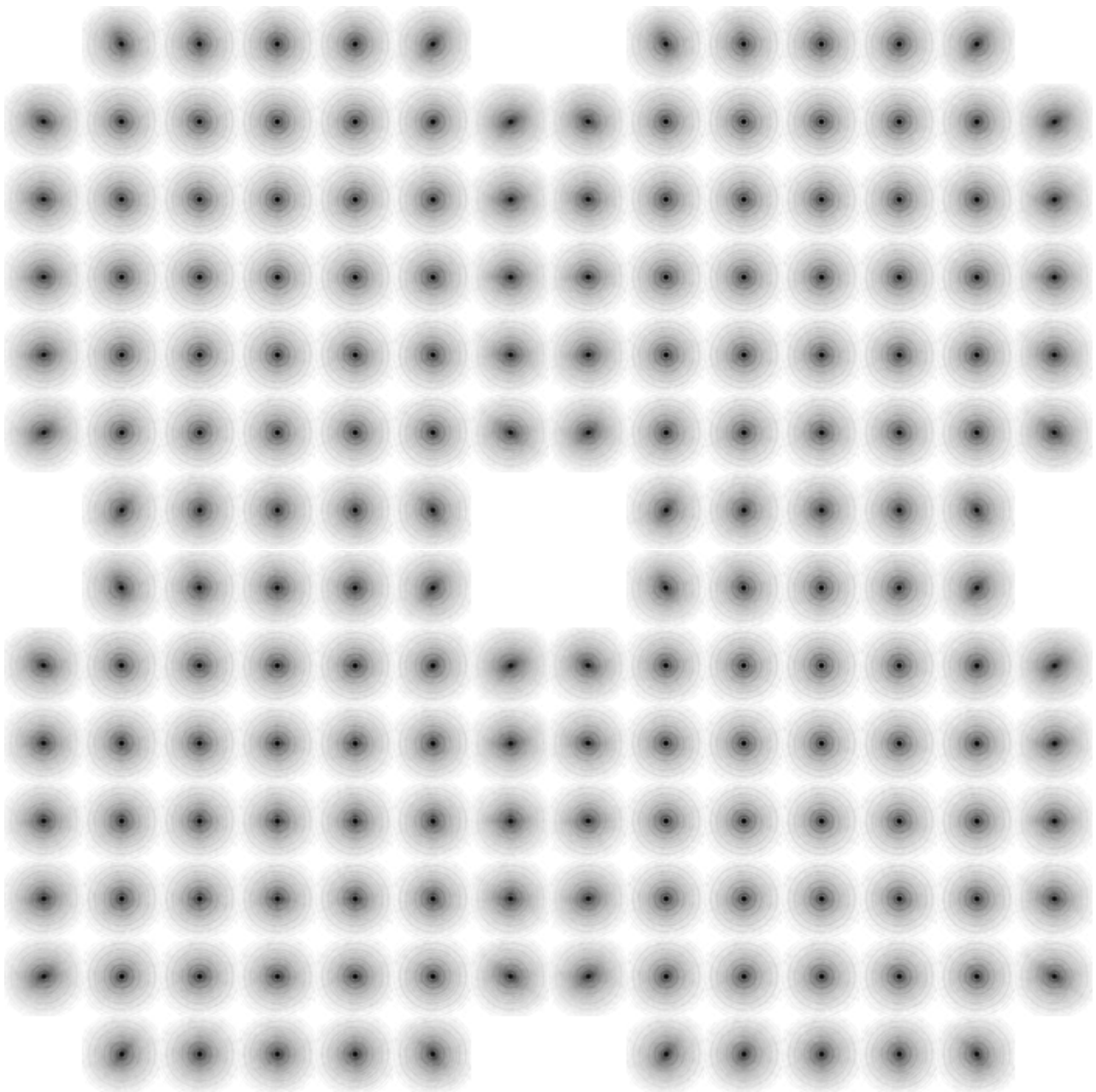


Figure 10: Array of PSFs at K-band for Configurations 1, 2, 3 and 4. The stretch is asinh and the pixel scale corresponds to Nyquist sampling.

Figure 9 plots the variation in K-band Strehl ratio and FWHM across the field. It is apparent that the best Strehl ratio is attained in the direction of the guide stars. For this reason, Configuration 1 produces the best on-axis Strehl ratio and should be preferred for narrow field science cases. The FWHM does not change significantly across the field.

Simulations were also run with the 25th and 75th percentile seeing conditions.

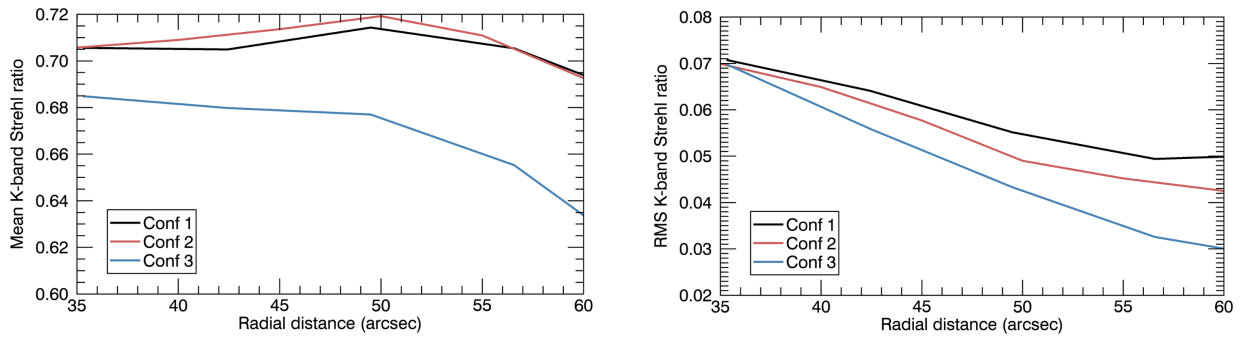


Figure 11: Simulated K-band Strehl ratio average and variation across the field for the three different configurations in 25th percentile seeing. The radial distance is the distance of the off-axis laser guide stars from the optical axis. The simulations were run at zenith.

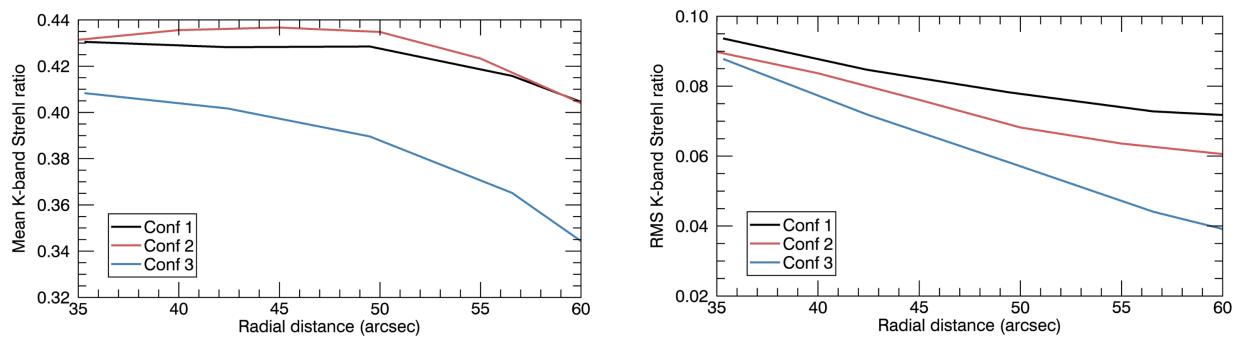


Figure 12: Simulated K-band Strehl ratio average and variation across the field for the three different configurations in 75th percentile seeing. The radial distance is the distance of the off-axis laser guide stars from the optical axis. The simulations were run at zenith.

Simulations using Configuration 3 were run using the median turbulence profile but varying the value of r_0 only (Figure 13 and Table 14).

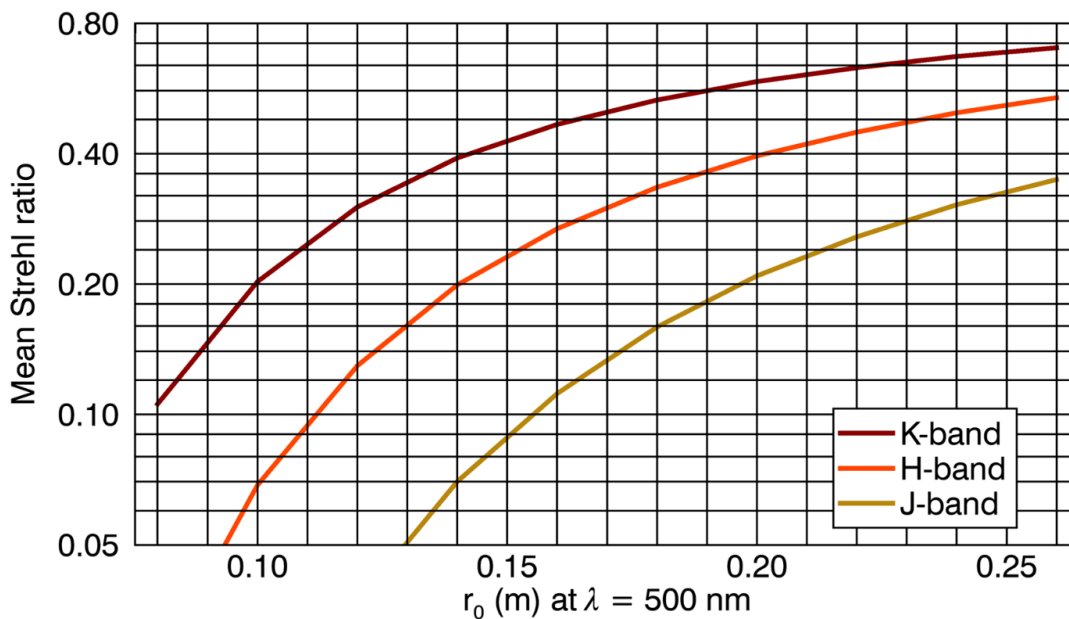


Figure 13: Simulated J-, H-, K-band Strehl ratio average for Configuration 3 for the median turbulence profile as a function of r_0 .

r_0	0.08	0.10	0.12	0.14	0.16	0.18	0.20	0.22	0.24	0.26
J-band	0.0057	0.0156	0.0367	0.0700	0.1118	0.1593	0.2090	0.2572	0.3051	0.3488
H-band	0.0260	0.0687	0.1296	0.1992	0.2686	0.3348	0.3956	0.4489	0.4975	0.5391
K-band	0.1057	0.2027	0.3014	0.3912	0.4676	0.5325	0.5872	0.6322	0.6711	0.7030

Figure 14: Simulated J-, H-, K-band Strehl ratio average for Configuration 3 for the median turbulence profile as a function of r_0 .

The simulations with median seeing were repeated at a zenith angle of 45° , with the results plotted in Figure 15 and tabulated in Tables 12, 14 and 13.

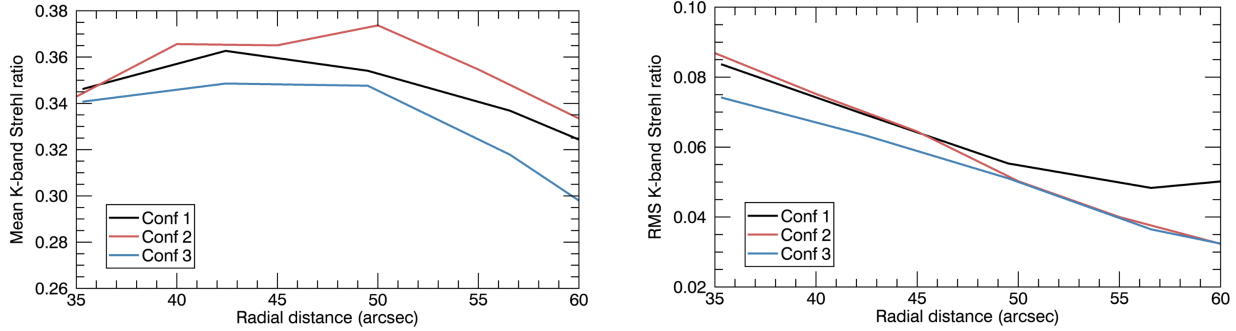


Figure 15: Simulated K-band Strehl ratio average and variation across the field for the three different configurations in median seeing. The radial distance is the distance of the off-axis laser guide stars from the optical axis. The simulations were run at a zenith angle of 45° .

The simulation results including fratricide for the three configurations are

Guide star locations [$\pm x, \pm x$]	25''	30''	35''	40''	45''
K-band Strehl	0.346 ± 0.084	0.363 ± 0.069	0.354 ± 0.055	0.337 ± 0.048	0.311 ± 0.052

Table 12: K-band Strehl ratio (average and standard deviation across the field) for Configuration 1.

Guide star dist	35''	40''	45''	50''	55''	60''
K-band Strehl	0.343 ± 0.087	0.365 ± 0.075	0.365 ± 0.064	0.374 ± 0.050	0.355 ± 0.040	0.333 ± 0.032

Table 13: K-band Strehl ratio (average and standard deviation across the field) for Configuration 2.

Guide star locations [$\pm x, \pm x$]	25''	30''	35''	40''	45''
K-band Strehl	0.341 ± 0.074	0.349 ± 0.063	0.348 ± 0.051	0.318 ± 0.036	0.277 ± 0.028

Table 14: K-band Strehl ratio (average and standard deviation across the field) for Configuration 3.

Figure 16 plots the variation in Strehl and FWHM across the field for the simulations at a zenith angle of 45° .

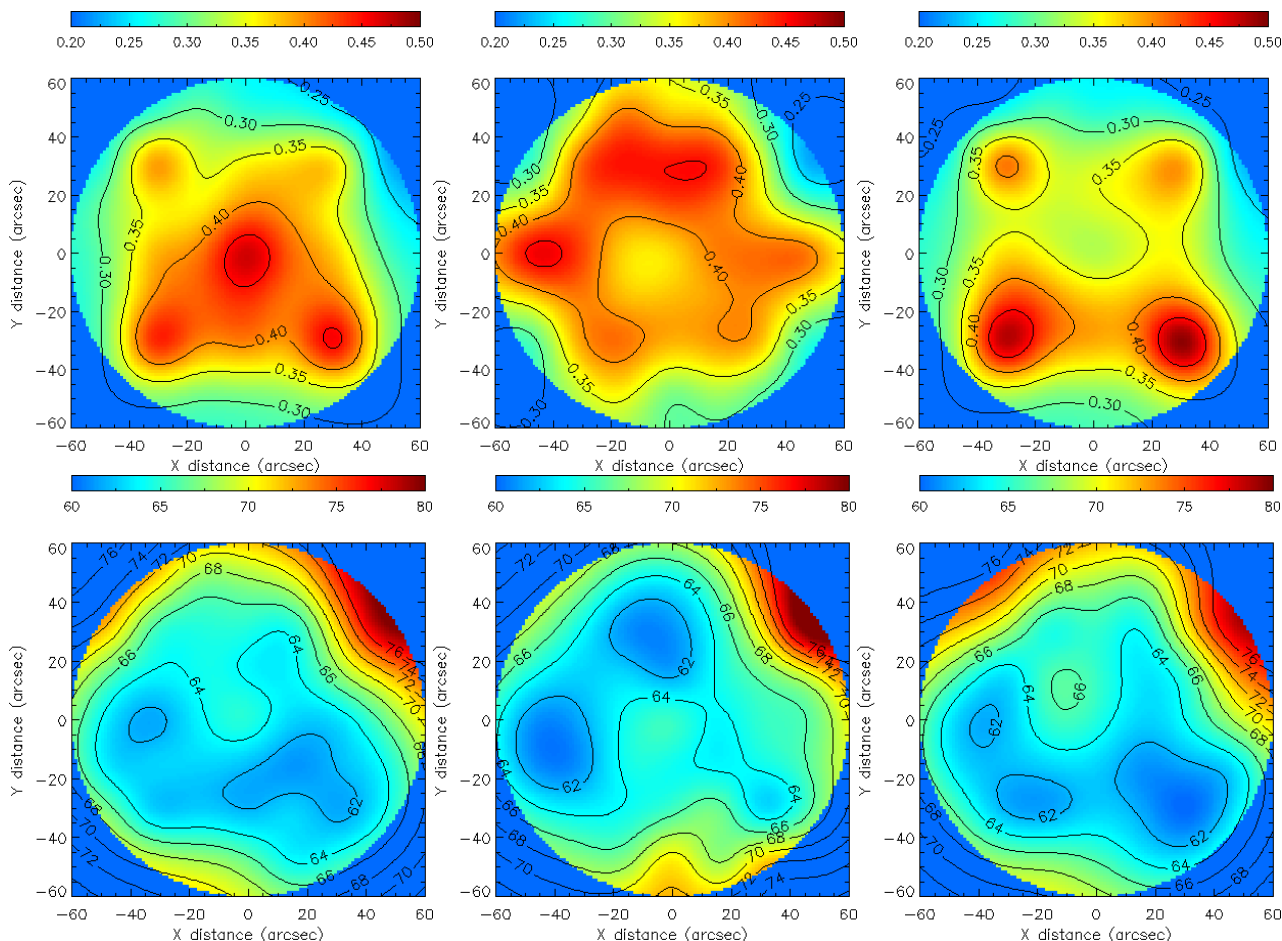


Figure 16: Variation in K-band Strehl ratio (top) and FWHM (bottom) across the field for Configurations 1, 2 and 3 for simulations at a zenith angle of 45° . The radial distance in all three cases was $50''$.

Simulations using Configuration 3 were run using the median turbulence profile and varying the zenith angle (Figure 17 and Table 15).

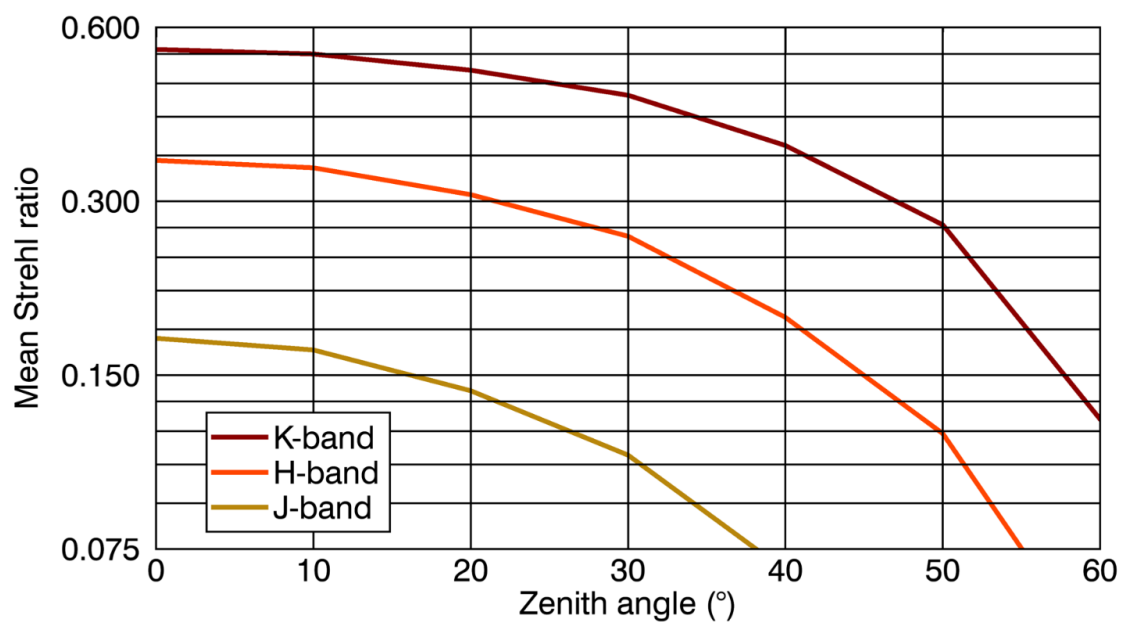


Figure 17: Simulated J-, H-, K-band Strehl ratio average for Configuration 3 for the median turbulence profile as a function of zenith angle.

Zenith angle	0°	10°	20°	30°	40°	50°	60°
J-band	0.1737	0.1658	0.1409	0.1090	0.0688	0.0392	0.0160
H-band	0.3531	0.3428	0.3080	0.2609	0.1888	0.1188	0.0476
K-band	0.5495	0.5396	0.5059	0.4578	0.3747	0.2731	0.1258

Table 15: Simulated J-, H-, K-band Strehl ratio average for Configuration 3 for the median turbulence profile as a function of zenith angle.

3.4 Interactuator spacing

A critical design decision is the number of DM actuators, since the DMs are very expensive and there are limited options. For this study, we will select Configuration 1 with a central guide star and four other guide stars at $[\pm 35'', \pm 35'']$. The simulations presented here have a WFS subaperture size the same as the interactuator spacing of DM0. In the first instance, DM14 has the same interactuator spacing as DM0, with the results presented in Table 16 and Figure 18. These simulations were run with ideal, noiseless WFSs in order to keep the simulations as closely comparable as possible. The results of the simulations using the smallest pitches could be slightly improved (1-2% relative Strehl) by optimizing the regularization. Nevertheless, the simulations clearly show that there is limited benefit in decreasing the DM pitch beyond 0.60 m.

DM pitch (m)	0.25	0.30	0.36	0.49	0.61	0.99
K-band Strehl	0.592±0.080	0.586±0.077	0.583±0.074	0.582±0.069	0.578±0.059	0.438±0.038

Table 16: K-band Strehl ratio (average and standard deviation across the field) as a function of interactuator spacing for both DM0 and DM14.

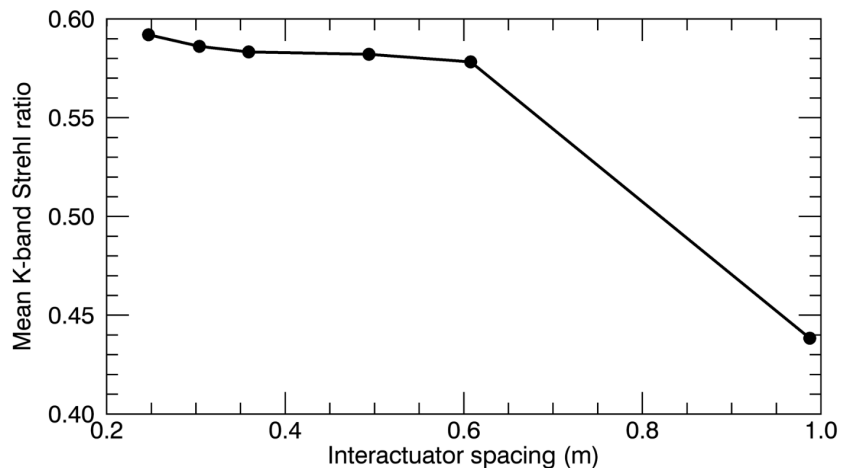


Figure 18: Simulated K-band Strehl ratio average across the field as a function of interactuator spacing of both DM0 and DM14.

The pitch of each DM can be optimized separately. Recall that GeMS has 50 cm interactuator spacing for DM0 (and DM4.5), while DM9 has an interactuator spacing of 100 cm. The pitch for DM0 was set to 50 cm, and the actuator density of DM14 was adjusted, with the results tabulated in Table 17.

DM pitch (m)	0.49	0.99	1.98
K-band Strehl	0.582±0.069	0.596±0.057	0.529±0.091

Table 17: K-band Strehl ratio (average and standard deviation across the field) as a function of interactor spacing for DM14. DM0 has an interactor spacing of 0.49 m.

Having an actuator density higher than that of GeMS does not improve the performance. The generalized fitting error is dominated by the number of conjugate altitudes and not by the number of actuators at each altitude. This is especially true of the high altitude DM, because the turbulence is distributed over a large range of altitudes (say, 4 km to 16 km) and cannot be well fit by a single DM.

3.5 DM conjugate altitude

The design includes a single high-altitude DM (nominally at 14 km in the simulations). If the secondary mirror is upgraded to a ASM, then the pupil DM is moved to a mid-altitude location. In this section, we investigate the performance as a function of DM conjugate altitude for both cases.

For these simulations, we need to increase the number of turbulence layers, otherwise the optimal DM altitude will coincide with the exact location one of the simulated turbulence layers.

The simulations in this section were run with the 50th percentile turbulence profile with the highest two layers each split into three, as shown in Table 18.

Elevation (km)	0	0.5	1	2	4	6	8	10	12	16	20
Wind speed (m/s)	5.6	5.8	6.25	7.57	13.31	19.1	19.1	19.1	12.1	12.1	12.1
Wind direction (°)	190	255	270	350	17	29	29	29	66	66	66
Turbulence fraction	0.456	0.130	0.044	0.051	0.117	0.031	0.031	0.031	0.037	0.037	0.037

Table 18: Turbulence profile used for the DM conjugate altitude simulations. The profile corresponds to the Mauna Kea 50th percentile with $r_0 = 0.186$ m. The upper two layers have each been subdivided into three layers.

The results of the simulations, plotted in Figure 19, show that the conjugate altitude for a 2 DM MCAO system should be between 8 km and 12 km for an observation at zenith and between 6 km and 9 km for an observation at a zenith angle of 45°. Paradoxically, the optimal altitude decreases with increasing zenith angle. This is probably because the high-altitude layers cannot be compensated at low elevations, so the correction is better when the DM is better matched to the mid-altitude layers. The dependence of performance on DM altitude is weak. Note that the Strehl ratios are all slightly lower because the turbulence distribution used in these simulations is less favorable to MCAO.

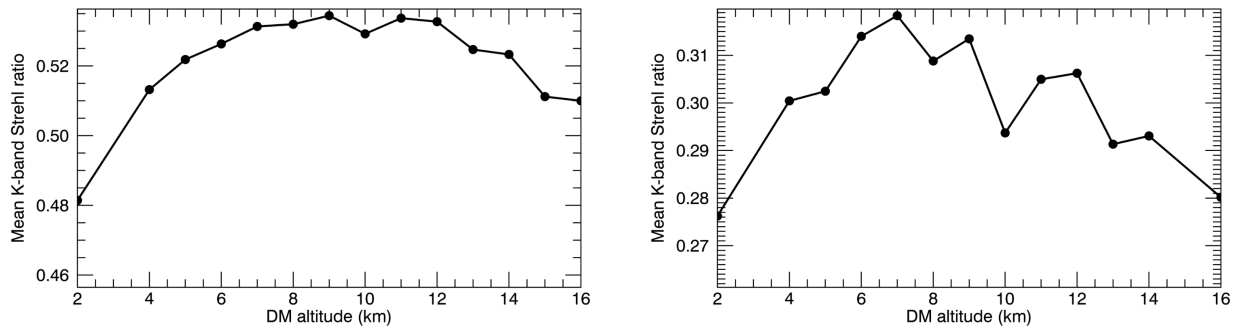


Figure 19: Simulated K-band Strehl ratio average across the field as a function of altitude of the high-altitude DM for a 2 DM system for observations at zenith (left) and a 45° zenith angle (right).

If an ASM is implemented, then the DM at the pupil will move up to 4.5 km. The K-band Strehl ratio as a function of the conjugation altitude of the third DM is plotted in Figure 20. Note that the simulations using three DMs have not yet been optimized.

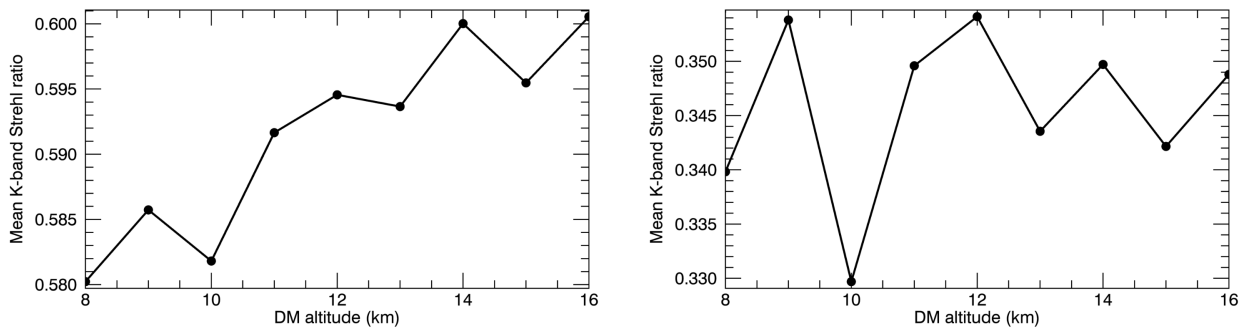


Figure 20: Simulated K-band Strehl ratio average across the field as a function of altitude of the high-altitude DM for a 3 DM system for observations at zenith (left) and a 45° zenith angle (right).

If only two DMs are used, we would place it at 7 or 8 km. However, in order to accommodate the shift of DM0 to an altitude of 4.5 km, we would want to place the DM at a slightly higher altitude of 9 or 10 km. The simulations all show a degraded performance at 10 km, but this is probably an artifact of insufficient layers in the tomographic reconstruction. This will be investigated. All things being equal, we want the DMs at as low an altitude as possible in order to reduce the number of actuators needed and the physical size of the DM.

As a comparison, we note that the MAVIS (MCAO Assisted Visible Imager and Spectrograph) design has DMs at 0 km, 4 km and 12 km, while GeMS originally had DMs at 0 km, 4.5 km and 9 km. NFIRAOS has two DMs, one conjugate to the ground and the other at 11.8 km. Note that MAVIS and NFIRAOS both have much smaller fields of view (30" x 30" and 34" x 34" respectively).

3.6 DM characteristics

In this section, we investigate the effect of two DM characteristics: hysteresis and influence function cross-coupling. Hysteresis has a negligible effect on performance, as illustrated by the constant Strehl ratio in Table 19.

Hysteresis	0%	1%	2%	4%	8%	16%
K-band Strehl	0.590±0.070	0.592±0.070	0.593±0.070	0.592±0.070	0.593±0.070	0.591±0.070

Table 19: K-band Strehl ratio (average and standard deviation across the field) as a function of hysteresis of DM0 and DM14.

Simulations were run with various values of DM cross-coupling, and it does not appear to be a critical parameter. Note that if the DM pitch is increased beyond the 50 cm value used here, then the conclusions may well be different.

Cross-coupling	0%	10%	15%	20%	25%	30%
K-band Strehl	0.585±0.071	0.588±0.070	0.590±0.070	0.593±0.068	0.593±0.068	0.591±0.067

Table 20: K-band Strehl ratio (average and standard deviation across the field) as a function of cross-coupling of DM0 and DM14.

The stroke requirements for the DM depends on multiple factors, including: worst seeing requirement, flatness of the DM, and aberrations on the science path (both common and non-common path). It is critical to have sufficient stroke, and this issue will not be addressed here.

3.7 LGS detector selection

There are two kinds of suitable LGS WFS detectors: an EMCCD camera such as the OCAM2, or a low read noise CCD, such as the CCID75. There are many factors that must be taken into consideration, such as the number of pixels and the physical pixel size, the cost, etc. Here, we just consider the noise performance, especially in the regime of low photon return.

The comparison is between a detector with a read noise of 0.5 e- and an excess noise factor of 1.41, with a detector with a read noise of 2 e- and an excess noise factor of 1. The photon return from the laser was reduced incrementally, to emulate observations with photon return. This could be due to a lower elevation, low sodium density or low laser power. The results, tabulated in Table 21, show that if the sodium return is greater than or equal to one quarter the expected return at zenith, then the low read noise CCD is to be preferred. If the return is much lower than this, then the EMCCD comes into its own. Note that the sodium return depends on many factors, such as zenith angle and azimuth, sodium density, etc.

Flux fraction	No noise	x1	x1/2	x1/4	x1/8	x1/16
OCAM2	0.600±0.069	0.591±0.069	0.581±0.068	0.562±0.068	0.527±0.066	0.470±0.065
CCID75	0.600±0.069	0.594±0.070	0.585±0.070	0.563±0.070	0.516±0.070	0.426±0.066

Table 21: K-band Strehl ratio (average and standard deviation across the field) as a function of flux reduction for an EMCCD and a low read noise CCD.

3.8 LGS WFS frame rate

Noiseless simulations were run with a range of frame rates to understand how the frame rate affects the performance (Table 22). The simulations were run with a one frame delay and a modest loop gain (0.4).

Frame rate	1000 Hz	500 Hz	250 Hz
K-band Strehl	0.562±0.051	0.554±0.050	0.552±0.050

Table 22: K-band Strehl ratio (average and standard deviation across the field) as a function of frame rate.

3.9 Pixel angular extent and number of pixels

The parameters used in the simulations that are relevant to the pixel extent are tabulated in Table 23.

Parameter	Value	Notes
Sodium density FWHM	8000 m	Elongation is
Intrinsic spot size FWHM	0.9''	Corresponds to M2=2
LLT diameter	0.5 m	
1/e ² diameter	0.3 m	
LLT r ₀	0.1 m	

Table 23: Parameters used for generating the spots in the LGS WFSs.

When observing at zenith, the spots produced using these assumptions lead to the spot pattern shown in Figure 21. The spot size for the most elongated spots is 1.28'' by 1.95''.



Figure 21: Spot pattern produced at zenith using the parameters in Table 23.

The parameters in in Table 23 are believed to be pessimistic, but the resulting spot size is still smaller than the values measured by the adaptive optics facility (AOF) at the VLT, which launches a Toptica LGSs using a TNO launch telescope. They typically measure the smallest spot size to have a FWHM of 1.5'', with the most elongated spots having a FWHM of 2.5''.¹⁵

The pixel size must be small enough to adequately sample the spots; it can be shown that for a Gaussian spot, the pixel size must be less than or equal to the FWHM,¹⁶ but Nyquist sampling is not

¹⁵Oberti, Sylvain, et al. "The AO in AOF." Adaptive Optics Systems VI. Vol. 10703. International Society for Optics and Photonics, 2018.

¹⁶Thomas, S., et al. "Comparison of centroid computation algorithms in a Shack–Hartmann sensor." Monthly Notices of the Royal Astronomical Society 371.1 (2006): 323-336.

required or beneficial. The simulations used 4x4 1.0" pixels, with excellent results. Experience at the WM Keck Observatory using a side-launched laser shows that the angular extent of the subapertures needs to be greater than 5" in order to avoid clipping of the most elongated spots. Having more pixels does not hurt if the read noise does not increase and a smart centroiding algorithm, such as the correlation algorithm or the weighted centroid, is selected.

If we use an OCAM2 camera, with 240x240 pixels and a very low read noise, we recommend a pixel scale of 0.8" with 8x8 pixels per subaperture. This design can accommodate up to 30x30 subapertures, and is consistent with the design of the AOF WFSs, which use 6x6 pixels per subaperture with a pixel scale of 0.83". If the CCID 75 is selected, we should use 8x8 0.9" pixels, since there is a larger penalty associated with reading more pixels. A smart centroiding algorithm (such as a weighted centroid or the correlation algorithm) will be needed in either case.

3.10 Dome seeing

Simulations were run at zenith using Configuration 3 with and without dome seeing (Table 24). The relative reduction in Strehl ratio due to dome seeing is 1.23%, which corresponds to a wavefront error of 39 nm.

K-band Strehl ratio	
No dome seeing	0.5495 ± 0.0508
With dome seeing	0.5427 ± 0.0506

Table 24: K-band Strehl ratio with and without dome seeing

3.11 Narrow-field performance

Since GNAO will replace Altair, it will also be used for narrow-field science cases. We compare the narrow-field performance of Configurations 1 and 3 with the off-axis guide stars situated at [35",35"] from the optical axis.

Three cases are considered for Configuration 3: the science target on-axis, the science target in the direction of one of the LGS guide stars, and the science target on-axis with one of the LGSs shifted on-axis (Table 25). The simulation results show that much better performance is attained for Configuration 1 compared to Configuration 3 with the science target on-axis. This can be partially mitigated by moving the science target to the location of one of the LGSs, and almost completely mitigated by moving one of the LGSs on-axis.

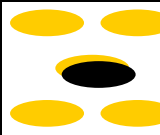
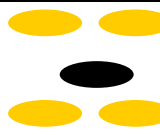
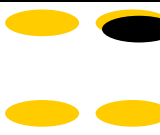
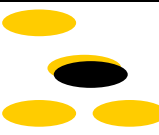
Configuration	1	3	3	3
Science target	[0",0"]	[0",0"]	[35",35"]	[0",0"]
LGS				
K-band Strehl	0.754	0.591	0.687	0.748

Table 25: K-band Strehl ratio for the narrow-field case. For Configuration 1, the science target is on-axis, while for Configuration 3, the science target is in the direction of one of the off-axis LGSs. Based on these results, it makes sense to implement Configuration 3 with five LGS WFSs and make the best use of the four LGSs depending on the science case. This would also allow a straightforward upgrade to Configuration 1.

If an ASM were present, a higher-order WFS would further improve the performance; the

optimization of the WFSs for narrow-field science is not addressed here.

3.12 Science atmospheric dispersion corrector

The current design has an atmospheric dispersion corrector (ADC) to correct for the dispersion of the science light due to differential atmospheric refraction (DAR) within the science band. For narrowband imaging, DAR has no effect. However, broadband images will be elongated in the elevation direction, because the shorter wavelengths in the passband are refracted more than the longer wavelengths. For the purposes of this exercise, we will assume a top-hat response for the photometric filters with the wavelength passbands in Table 26.

Wavelength (microns)	Minimum	Center	Maximum
J-band	1.170	1.250	1.330
H-band	1.490	1.635	1.780
K-band	2.030	2.200	2.370

Table 26: Wavelength passband for photometric filters.¹⁷

The dispersion as a function of wavelength is calculated using a Python interface¹⁸ to the SLALIB library,¹⁹ with the parameters tabulated in Table 27.

Parameter	Value
Elevation	4213 m
Temperature	273 K
Pressure	605 mb
Relative humidity	50%

Table 27: Parameters used for refraction calculations

The dispersion as a function of wavelength for two different zenith angles is plotted in Figure 22. At a zenith angle of 45°, the total dispersion across the J-, H- and K-bands is 33.4 mas, 27.2 mas and 13.0 mas respectively. The dispersion is proportional to $\tan(\theta_z)$.

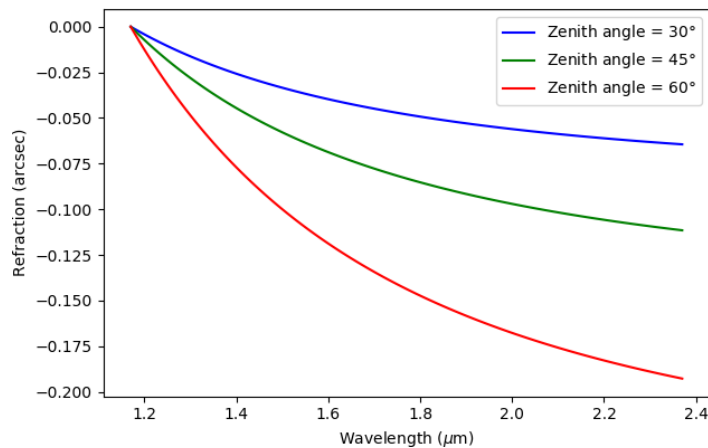


Figure 22: Dispersion across J-, H- and K-bands on Mauna Kea for zenith angles of 30°, 45° and 60°.

¹⁷http://www.ifa.hawaii.edu/~tokunaga/MKO-NIR_filter_set.html

¹⁸<https://pypi.org/project/pySLALIB/>

¹⁹<http://star-www.rl.ac.uk/star/docs/sun67.htx/sun67.html>

Monochromatic PSFs at a range of wavelengths within each filter were generated. The PSFs were displaced with respect to each other to simulate the dispersion, and then coadded to create broadband images. As a representative case, we select the on-axis star for the widefield case using Configuration 3 at zenith angle of 45°. The PSFs generated with a 20 mas pixel size with and without atmospheric dispersion are displayed in Figure 23. The relative Strehl reduction due to dispersion is 7.4%, 8.9% and 1.2% at J-, H- and K-band respectively.

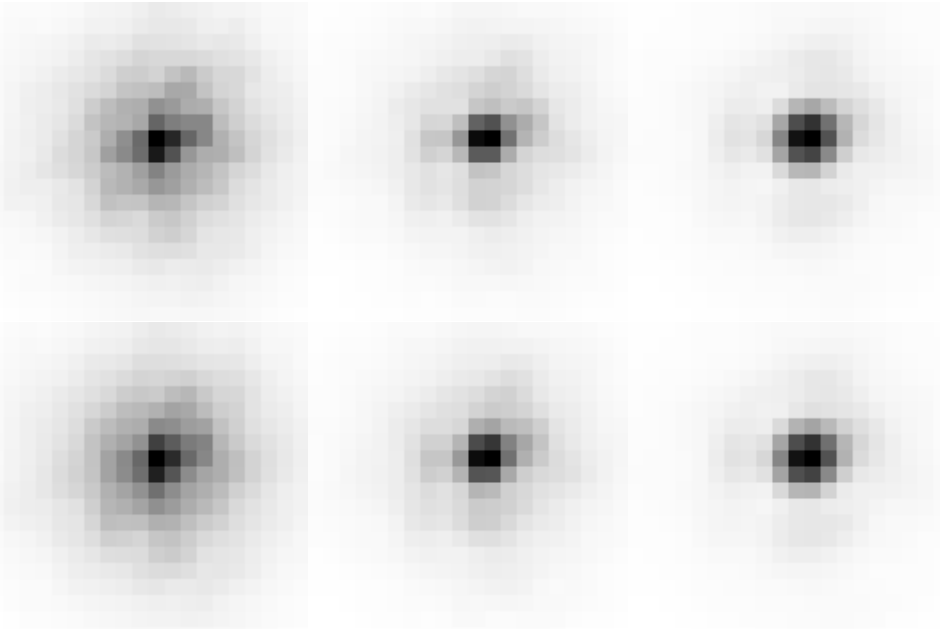


Figure 23: J-, H- and K-band undispersed PSFs (top) and dispersed PSFs (bottom) generated with a 20 mas pixel scale at a zenith angle of 45°.

The relative reduction in Strehl for different zenith angles, and also for the case where the correction is optimized for the on-axis location only (using the triangular constellation in the last column of Table 25). A 10% relative reduction in Strehl means that the Strehl drops from 0.30 to 0.27, for example. Based on these results, tabulated in Table 28, it is not clear if an ADC on the science path is needed. An ADC is useful when the correction is good and the dispersion is large. However, the wide-field correction at low elevations is not very good, so the ADC does not help much. The narrow-field case benefits more from an ADC.

Field of view	Zenith angle	J-band	H-band	K-band
Wide field	30°	5.4%	4.3%	0.5%
Wide field	45°	7.4%	8.9%	1.2%
Wide field	60°	6.9%	5.1%	2.0%
Narrow field	30°	7.3%	4.5%	0.5%
Narrow field	45°	12.4%	7.6%	0.8%
Narrow field	60°	15.3%	13.3%	2.5%

Table 28: Relative reduction in on-axis Strehl ratio as a function of zenith angle for the case where we optimize the correction for a 2' diameter field and on-axis only.

4 NGS guide star performance

4.1 Limiting magnitude

Simulations were run to determine the tip-tilt error at the location of the natural guide star as a function of guide star magnitude. For speed of simulation, the simulations were run without any DM correction.

There were three disturbances in the simulations: the atmospheric turbulence (see Section 5), a disturbance based on the Altair circular buffers (see Section 11) and a constant centroid offset of [0.04", 0.08"], to which the NGS spot is driven.

The guide star magnitude was varied between $m_R=12$ and $m_R=19$, with the integration varied between 62.5 Hz and 1000 Hz to find the optimal setting. In all cases, the loop gain was 0.4 and the compute delay was 1 ms. The tip-tilt error was determined by measuring the true tip-tilt error at 1 kHz using a noiseless tip-tilt sensor.

The tip-tilt error as a function of frame rate for a bright natural guide star is plotted in Figure 24. It can be seen that even at 1000 Hz, we are unable to correct for the telescope-induced vibrations. Running the loop more slowly has little effect on the performance. Advanced controllers could help reduce the error when using bright guide stars.

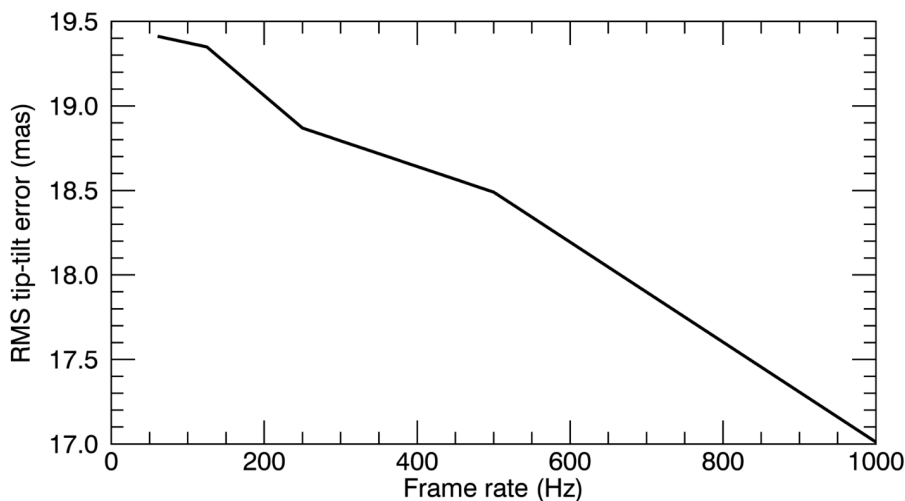


Figure 24: Tip-tilt error as a function of frame rate with coarsely optimized loop gain.

The tip-tilt error as a function of guide star magnitude (using the optimal frame rate and loop gain for the star) is plotted in Figure 25. It appears that the limiting magnitude of the tip-tilt sensor is around $m_R=19$. This will depend on the seeing and the sky background.

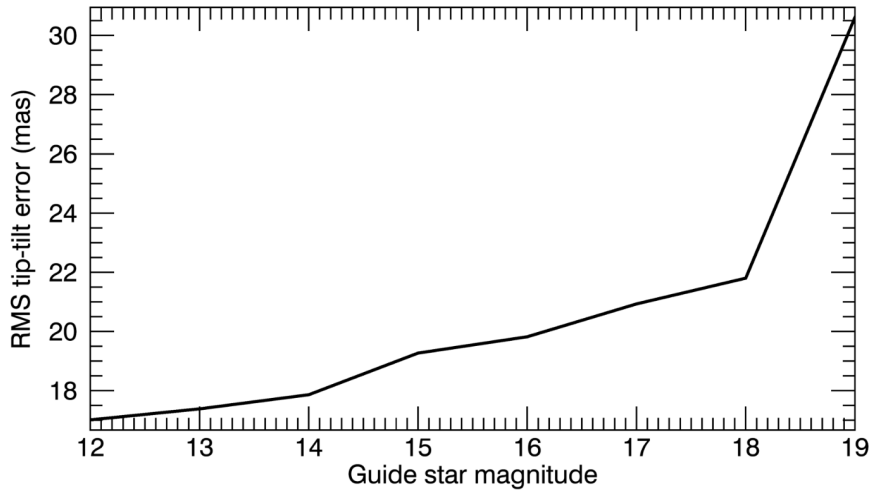


Figure 25: Tip-tilt error as a function of guide star magnitude with the frame rate and loop gain coarsely optimized for each guide star magnitude.

4.2 Tip-tilt disturbances

Simulations were run at 1000 Hz with no noise using 24 circular buffers obtained on 23 different nights. The RMS tip-tilt errors, plotted in Figure 26, show that the circular buffers in Section 11, is representative of the conditions at the telescope (slightly worse than median).

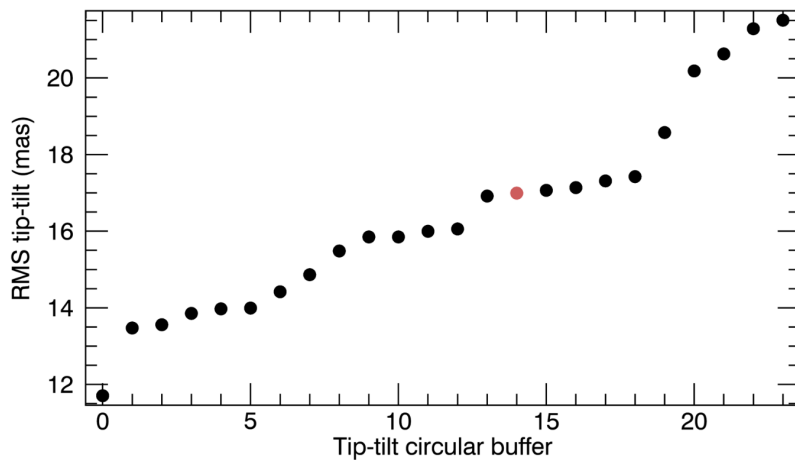


Figure 26: RMS tip-tilt (mas) for each of the circular buffers. The circular buffer presented in Section 11 is plotted in red.

4.3 Effect of atmospheric dispersion compensation

The same simulations were run at different elevations to understand how atmospheric dispersion affects the performance. The dispersion as a function of wavelength and zenith angle is plotted in Figure 27. It can be seen that there is up to 1" of dispersion between 0.4 microns and 0.9 microns at a zenith angle of 45°, causing an increase in spot size and a decrease in centroiding accuracy. Simulations were run to understand the effect this has on the limiting magnitude.

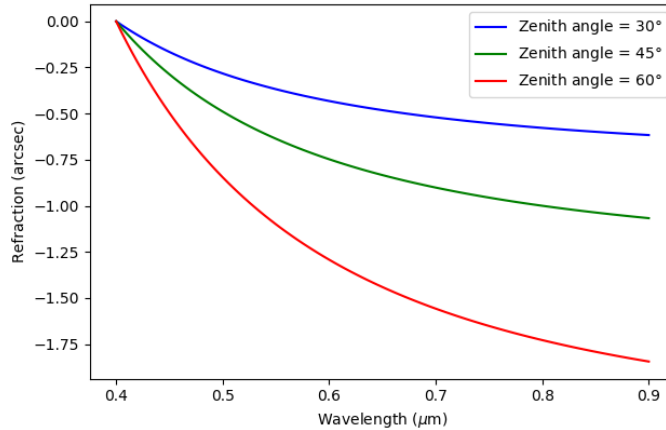


Figure 27: Dispersion from 0.4 microns to 0.9 microns on Mauna Kea for zenith angles of 30°, 45° and 60°.

The simulation tool YAO does not currently support multi-wavelength WFSs. The effect of dispersion was simulated by convolving the seeing-limited spot on the NGS WFS, which is calculated at a wavelength of 640 nm, with a dispersion ranging from 400 nm to 900 nm. The flux was assumed to be evenly distributed over this passband, which is a pessimistic assumption.



Figure 28: Instantaneous PSF on the tip-tilt sensor at a 45° zenith angle without (left) and with (right) dispersion.

The tip-tilt error as a function of guide star magnitude at zenith angles of 30° and 45°, without an ADC and with a perfect ADC, is plotted in Figure 29.

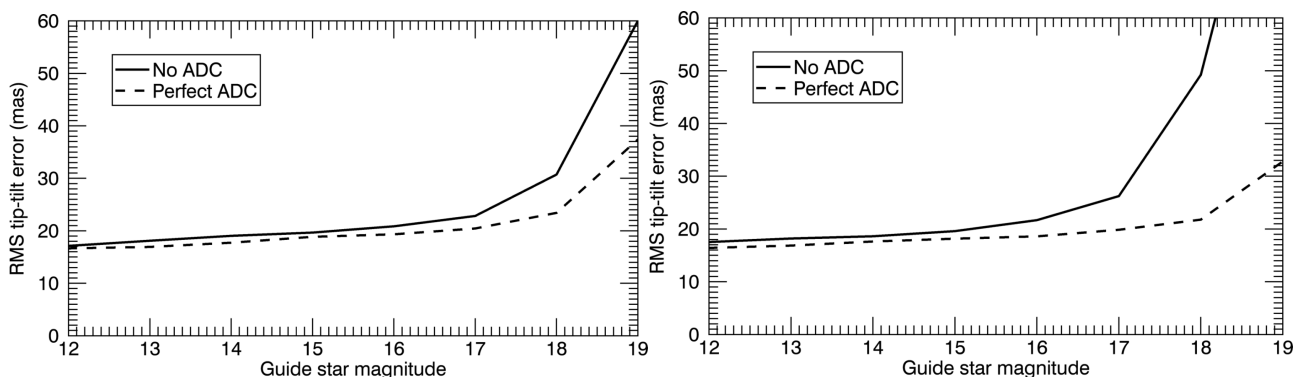


Figure 29: Tip-tilt error as a function of guide star magnitude with the frame rate and loop gain coarsely optimized for each guide star magnitude. The zenith angle is 30° (left) and 45° (right), and the simulations are performed assuming a perfect ADC and no ADC.

The dispersion leads to a large degradation in performance at low elevations. Future work could include a custom YAO module that simulates the wavelength-dependent physical optics propagation and the dispersion in the tip-tilt sensor.

4.4 Sky coverage calculations

The term “sky coverage” does not have a clear definition in MCAO. A single star is sufficient to close to the tip-tilt loop and also to measure the variations in the sodium layer. While having more stars allows for the correction of field-dependent tip-tilt, it is not always true that three stars will produce better performance than a single star. For example, a bright star at the center of the field leads to better performance than three badly distributed faint stars.

Code was written to calculate the tip-tilt error across the field as a function of the location of the guide stars. The code also includes a measurement error associated with each star. The measurement error depends on the guide star magnitude as well as the control law. Optimizing the sum of the bandwidth error, measurement error and tip-tilt tomographic error is beyond the scope of this study. To see how the tip-tilt error depends on the number and location of the stars, the tip-tilt error due to anisokinetism was calculated for few asterisms at zenith, with the tip-tilt error as a function of position in the field plotted in Figure 30.

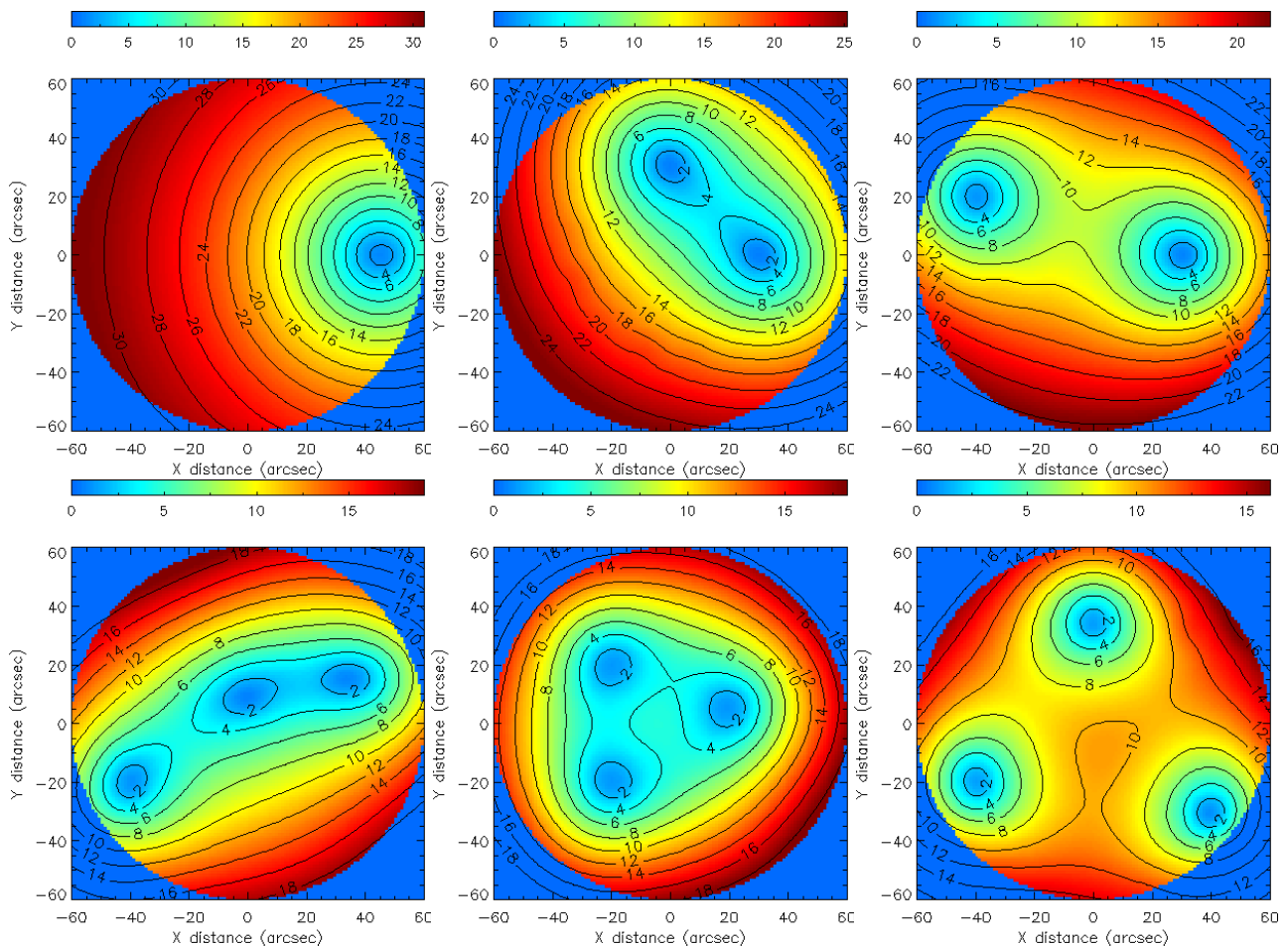


Figure 30: Anisokinetic angle over the 2' diameter field of view for various asterisms with one, two or three tip-tilt stars. The bottom right hand figure corresponds to the default tip-tilt asterism used in all of the simulations. The location of the tip-tilt star is evident from the plots!

We can see that the error is very sensitive to the distribution of the stars, and that a sky coverage calculation should compute the average and maximum tip-tilt error across the field for the optimal asterism, taking the measurement noise into account, rather than simply finding the number of stars. This calculation will take place in the future.

The sky coverage calculations are performed in the following manner. 1000 random pointings on the sky are created at random times at night throughout the course of the whole year. The elevation

is restricted to the range 45° to 90°. The R-band magnitude of stars within a 1 arcmin radius of each pointing are extracted from the USNO-B1.0 catalog, believed to provide all-sky coverage, completeness down to $m_V = 21$, 0.2 arcsecond astrometric accuracy at J2000, 0.3 magnitude photometric accuracy in up to five colors.²⁰ Stars that have unknown magnitude or are too faint are discarded.

The Gaia catalog was also used to compute the sky coverage. R-band magnitudes were estimated based on the magnitudes G_{mag} , G_{bp} and G_{rp} from the Gaia catalog using the following formula:

$$m_R = G_{mag} + 0.003226 - 0.3833(G_{bp} - G_{rp}) + 0.1345(G_{bp} - G_{rp})^2 \quad (1)$$

We record the number of sufficiently bright stars in Table 29.

Stellar magnitude	0 stars	≥1 star	≥2 stars	≥3 stars	0 stars	≥1 star	≥2 stars	≥3 stars
$m_R \leq 18.0$	0.409	0.591	0.182	0.074	0.473	0.527	0.189	0.052
$m_R \leq 18.5$	0.331	0.669	0.352	0.131	0.399	0.601	0.251	0.070
$m_R \leq 19.0$	0.220	0.780	0.485	0.257	0.322	0.678	0.336	0.126

Table 29: Probability of finding sufficiently bright stars in the field as a function of limiting magnitude using the USNO catalog (left) and the Gaia catalog (right).

We are also interested in finding the fraction of fields with “good” asterisms. A good three star asterism must follow these somewhat arbitrary criteria:

- any two stars must be separated by 40” or more
- the three stars must form a triangle with a minimum angle greater than 25°.

A “good” two-star asterism only needs to meet the first condition.

The probability of finding good asterisms is tabulated in Table 30. Note that if we have a “bad” three-star asterism, we would still use all three stars, but the performance would be closer to the performance of a two-star asterism.

Stellar magnitude	0 stars	≥1 star	≥2 stars	≥3 stars	0 stars	≥1 star	≥2 stars	≥3 stars
$m_R \leq 18.0$	0.409	0.591	0.184	0.013	0.473	0.527	0.138	0.013
$m_R \leq 18.5$	0.331	0.405	0.231	0.033	0.399	0.601	0.186	0.015
$m_R \leq 19.0$	0.220	0.780	0.387	0.087	0.322	0.678	0.263	0.038

Table 30: Probability of finding good asterisms with sufficiently bright stars in the field as a function of limiting magnitude

The science requirements are defined in terms of sky coverage at the North Galactic Pole:
GNAO-SCI-005: GNAO shall operate with at least 60% sky coverage with 1 NGS at galactic pole.
GNAO-SCI-006: GNAO shall operate with 20% sky coverage with 3 NGSs at galactic pole.

The number of sufficiently bright stars in fields randomly distributed within 5° of the North Galactic Pole (Figure 31) is tabulated in Tables 31 and 32. The requirements are almost met if the limiting magnitude is $m_R=19$.

²⁰<http://tdc-www.harvard.edu/catalogs/ub1.html>

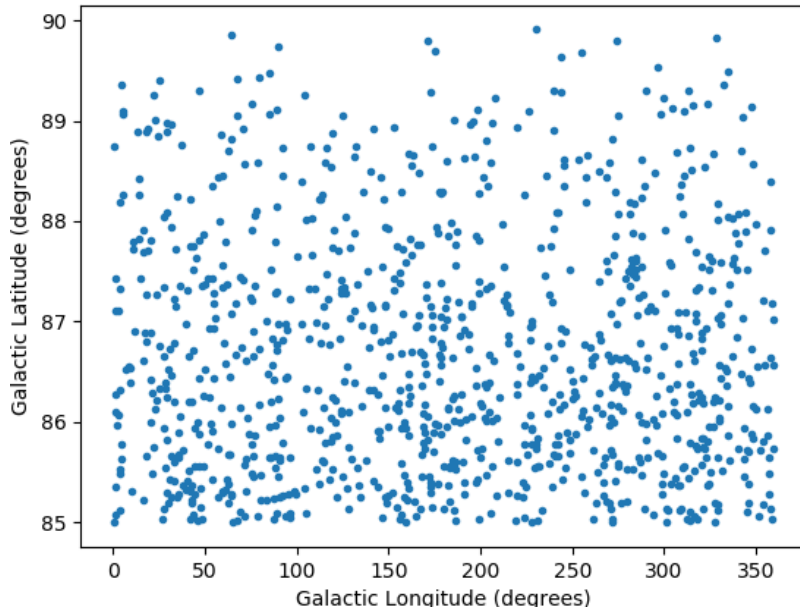


Figure 31: Random distribution of stars within 5° of the North Galactic Pole.

Stellar magnitude	0 stars	≥ 1 star	≥ 2 stars	≥ 3 stars	0 stars	≥ 1 star	≥ 2 stars	≥ 3 stars
$m_R \leq 18.0$	0.502	0.498	0.196	0.052	0.555	0.445	0.137	0.026
$m_R \leq 18.5$	0.395	0.327	0.165	0.113	0.455	0.545	0.191	0.038
$m_R \leq 19.0$	0.303	0.697	0.395	0.191	0.419	0.581	0.250	0.072

Table 31: Probability of finding sufficiently bright stars in the field as a function of limiting magnitude using the USNO catalog (left) and the Gaia catalog (right) within 5° of the North Galactic Pole.

Stellar magnitude	0 stars	≥ 1 star	≥ 2 stars	≥ 3 stars	0 stars	≥ 1 star	≥ 2 stars	≥ 3 stars
$m_R \leq 18.0$	0.502	0.498	0.129	0.021	0.555	0.445	0.093	0.006
$m_R \leq 18.5$	0.395	0.605	0.200	0.030	0.455	0.545	0.129	0.010
$m_R \leq 19.0$	0.303	0.697	0.312	0.061	0.419	0.581	0.182	0.023

Table 32: Probability of finding good asterisms with sufficiently bright stars in the field as a function of limiting magnitude using the USNO catalog (left) and the Gaia catalog (right) within 5° of the North Galactic Pole.

These results should be compared against results obtained using simulated star fields. In the future, a tool that estimates the tip-tilt error across the field of view of the instrument as a function of asterism will be written.

Another consideration is the total flux of the stars in the passband. Here, we used the R-band magnitude as a proxy for the magnitude of the star across the VRI-bands. However, the magnitude is not constant across the three bands. Using the TESS Input Catalog (TIC), we compared stellar magnitudes for stars where the R-band and I-band are also catalogued, we find median values of $m_V - m_R = 0.32$ and $m_V - m_I = 0.92$ (see Figure 32).

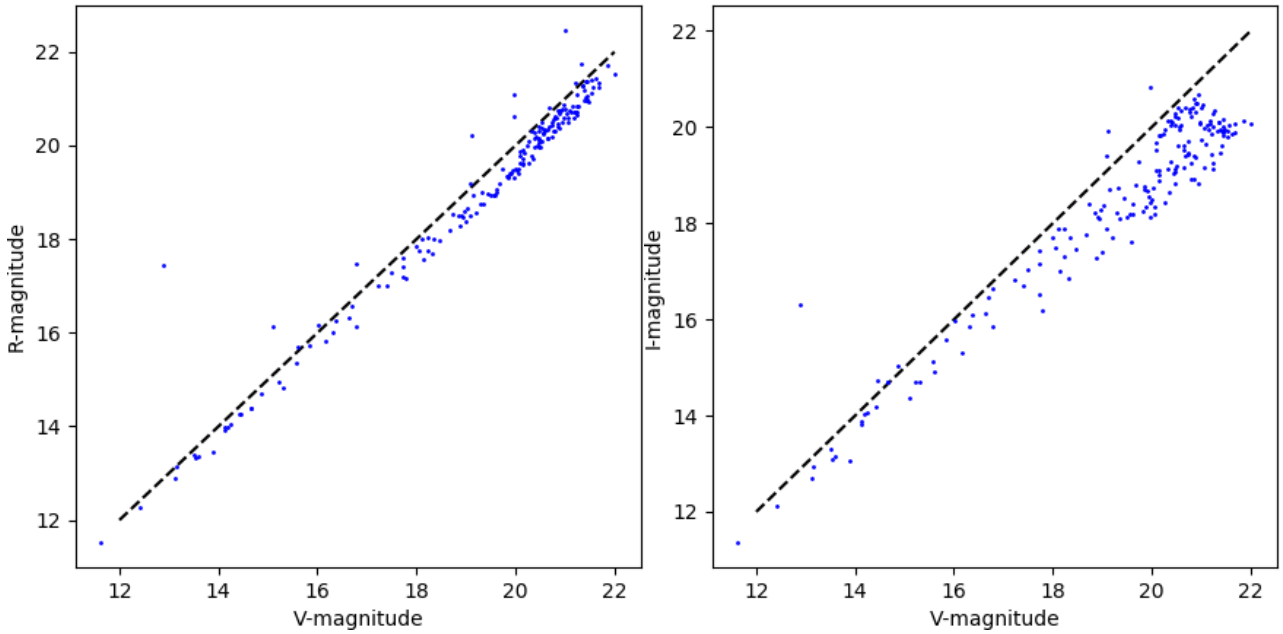


Figure 32: V-band vs R-band magnitudes (left) and V-band vs I-band magnitudes (right) using the TESS Input Catalog.

5 Semi-analytical calculations

In order to understand the limitations imposed by the design choices and to help flesh out the error budget, semi-analytical calculations of the high-order tomographic error, the classical fitting error, and the generalized fitting error have been programmed.

5.1 High-order tomographic error

The tomographic error is the error due to lack of knowledge about the wavefront. This limitation results from the number and location of the laser guide stars as well as the sodium altitude. To calculate the high-order tomographic error we compute the covariance matrices for the wavefront in the direction of the laser guide stars, C_{xx} , the covariance matrix for the wavefront in the direction of the science targets, C_{xx} , and the cross-covariance values C_{ax} . The calculation of the covariance matrices is described in van Dam et al.²¹ The measurement noise covariance, C_{nn} , is a diagonal matrix with a value of 0.0001.

The wavefront in the direction of the science targets is estimated based on the WFS measurements as follows:

$$\hat{\mathbf{a}} = \mathbf{C}_{ax}(\mathbf{C}_{xx} + \mathbf{C}_{nn})^{-1}\mathbf{x} \quad (2)$$

And the residual, r , which is the difference between the true and the estimated value, has a covariance matrix given by

$$\mathbf{C}_{rr} = \mathbf{C}_{aa} - \mathbf{C}_{ax}(\mathbf{C}_{xx} + \mathbf{C}_{nn})^{-1}\mathbf{C}_{xa} \quad (3)$$

The piston and tip-tilt contribution are removed from C_{rr} , and the diagonal values represent the variance of the residuals.

We now use this formalism to evaluate the tomographic errors for the different wavefront sensing configurations. In what follows, we report the square root of the squared wavefront error averaged over the whole field. The tomographic error for Configurations 1 and 3 is plotted in Figure 33.

²¹Van Dam, Marcos, et al. "Wavefront Reconstruction for a Natural Guide Star Ground Layer Adaptive Optics System on the Giant Magellan Telescope." Adaptive Optics for Extremely Large Telescopes III (2013).

These plots are consistent with the simulation results but can be calculated about two orders of magnitude faster.

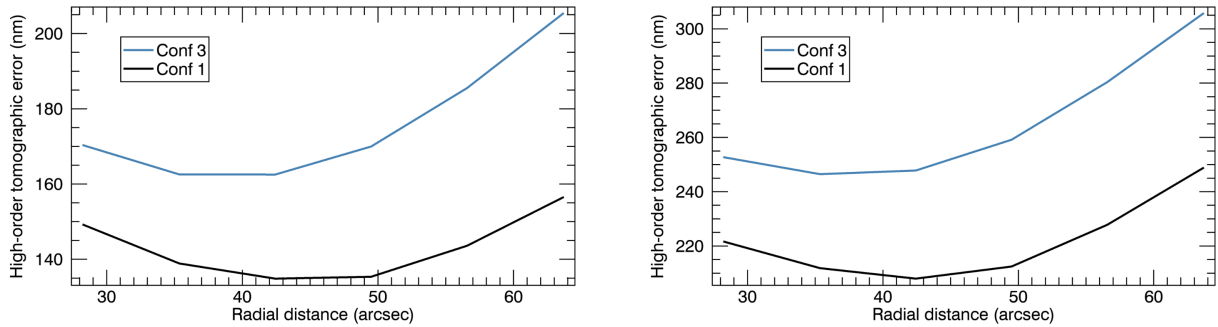


Figure 33: High-order tomographic error as a function of radial distance of the guide stars using Configurations 1 and 3. The error is calculated at zenith (left) and at a 45° zenith angle (right) with the median turbulence profile.

The tomographic error as a function of position in the field is another output of this formalism, as shown in Figure 34.

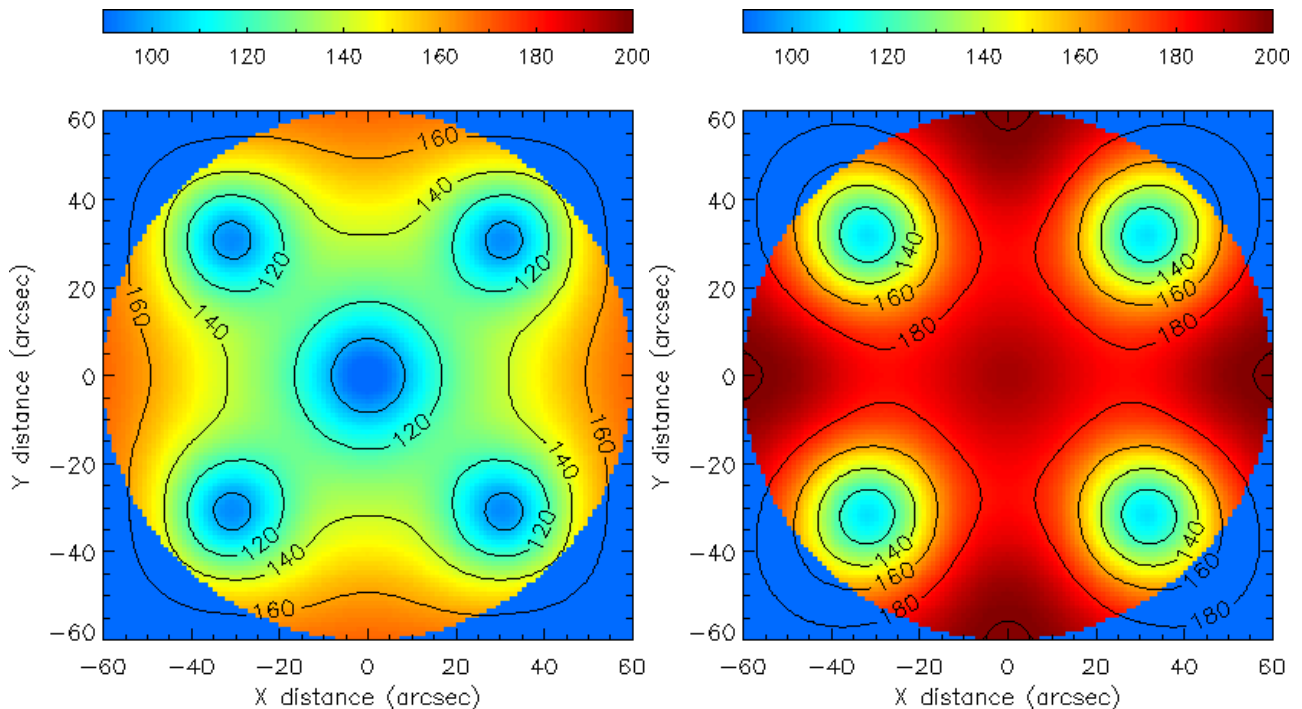


Figure 34: High-order tomographic error (in nm) as a function of of position of the field for Configurations 1 (left) and 3 (right). The radial distance of the outer guide stars is 49.5”. The calculation is performed at zenith with the median turbulence profile.

5.2 Classical fitting error

The “classical” fitting error is the residual wavefront error due to the limited actuator density. This is an important error term for single conjugate AO systems, but is superseded by the generalized fitting error for MCAO (see Section 39). We include it here both to show that the actuator density is not a significant error term and for comparison with the generalized fitting error, which includes the effect of the actuator density in not only the x and y directions, but also in the z -direction.

The fitting error is calculated as follows. We generate 300 random phase screens with the correct statistics to represent the atmospheric turbulence. The DM actuators commands are set to the value

that best cancels the aberrations along the optical axis. The residual is the fitting error.

For 17x17 actuators across the pupil, we calculate the fitting error to be 86 nm.

5.3 Generalized fitting error

The generalized fitting error is the error in correcting the 3D volume of turbulence. For existing MCAO systems, it is dominated by the sampling of the turbulence in the z-direction.

The generalized fitting error is computed in a manner similar to the classical fitting error. The same phase screens are generated. The DM commands are set to cancel the wavefront in the direction of 45 science targets evenly distributed over the science field of view. This assumes perfect knowledge of the wavefront. The residual wavefront along the direction of each of the science targets is then computed.

The generalized fitting error as a function of altitude of the high-altitude DM for a 2 DM and a 3 DM system is plotted in Figure 35. The relative insensitivity to DM altitude was also found in the simulations. For a 2 DM system, the high-altitude DM at around 11 km yields the best performance. For a 3 DM system, the high altitude DM should be no lower than 11 km.

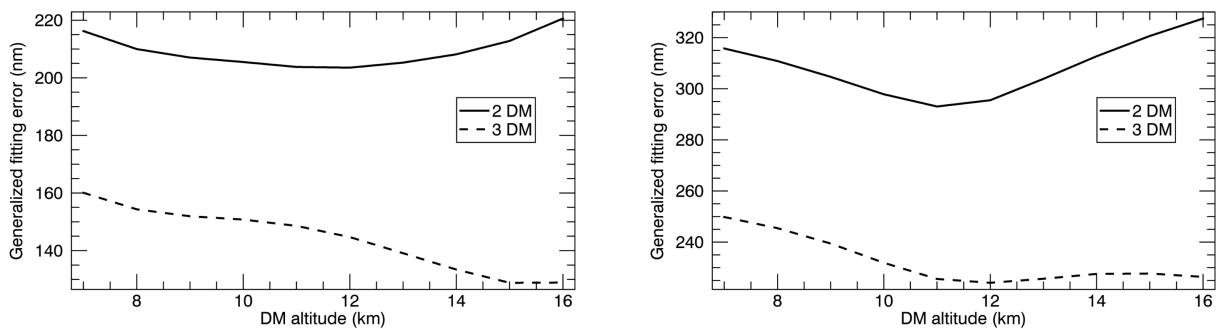


Figure 35: Generalized fitting error as a function of DM altitude for the 2 DM and 3 DM case at zenith (left) and a 45° zenith angle (right).

The generalized fitting error as a function of position in the field is shown in Figures 36 and 37 for observations at a zenith angle of 0° and 45° respectively. The figures show how a third DM improves the correction everywhere and increases the region over which the correction is constant.

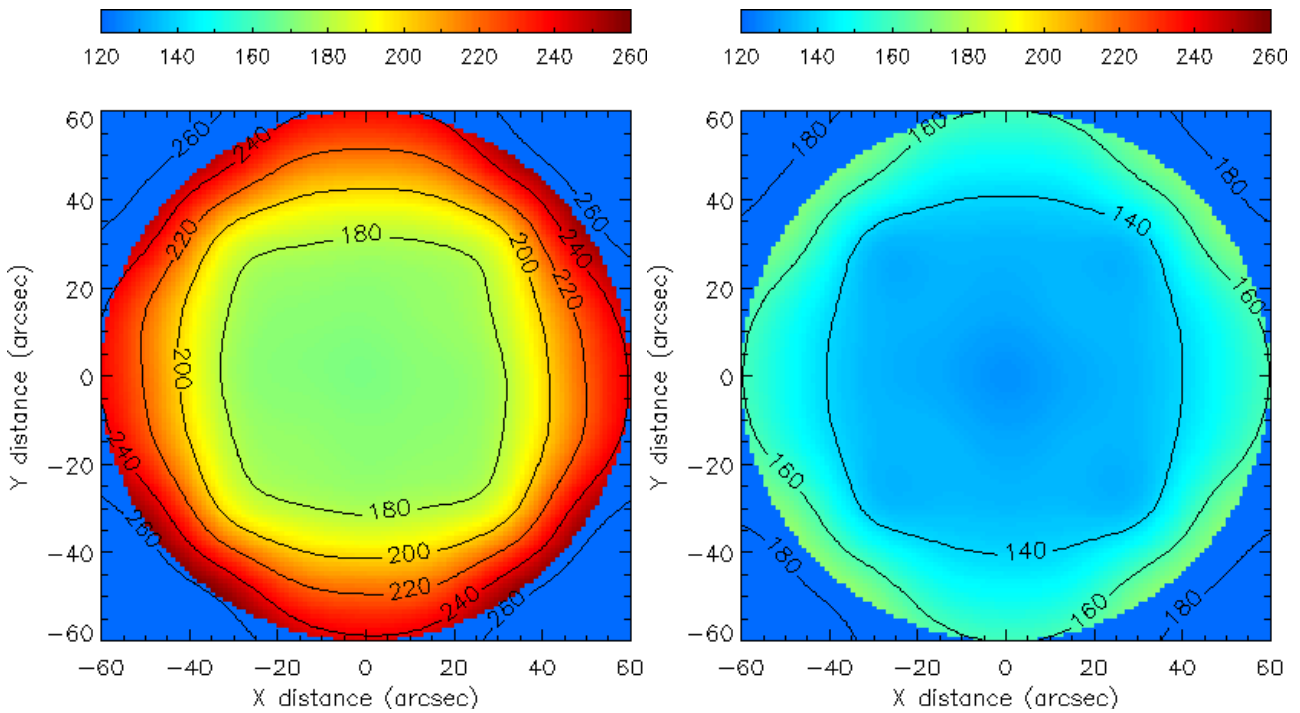


Figure 36: Generalized fitting error at zenith for two DMs (left) and three DMs (right). The high-altitude DM is at 12 km, and the mid-altitude DM is at 4 km.

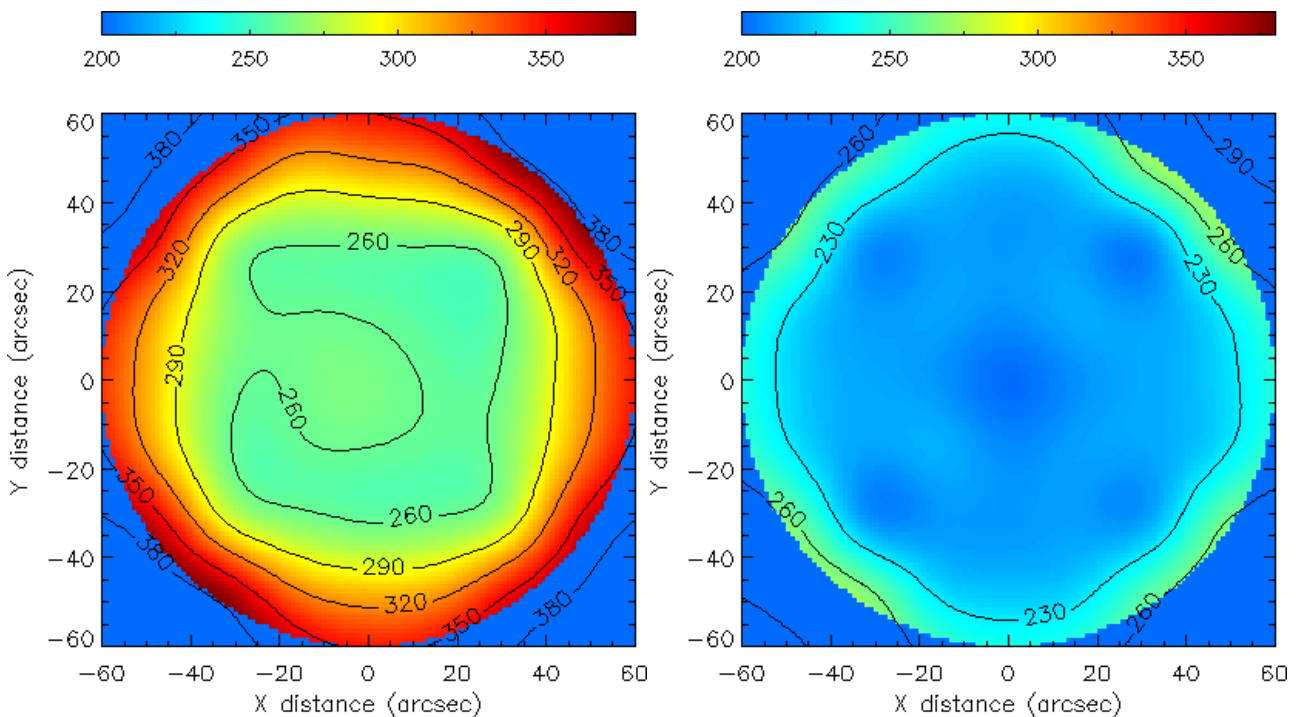


Figure 37: Generalized fitting error at a 45° zenith angle for two DMs (left) and three DMs (right). The high-altitude DM is at 12 km, and the mid-altitude DM is at 4 km.

We also want to confirm that we do not need the same actuator density for the high altitude DM. The generalized fitting error as a function of DM pitch is for a 2 DM and a 3 DM system is tabulated in Tables 33 and 34 respectively. It is clear that the DM conjugate to the ground requires fine sampling, while the high-altitude DMs do not. The reason for this is that as the altitude increases, the mismatch in altitude between the DM and the turbulence also increases so the high spatial frequencies cannot be corrected over a large field of view.

Zenith angle	DM altitude	400 cm	200 cm	100 cm	50 cm
0°	0 km	349.5	277.9	223.8	203.5
0°	12 km	251.7	212.8	203.5	203.5
45°	0 km	453.8	362.7	314.7	295.5
45°	12 km	349.5	308.2	296.9	295.5

Table 33: Generalized fitting error as a function of interactuator pitch and zenith angle for a 2 DM system. The interactuator pitch is changed one DM at a time.

Zenith angle	DM altitude	400 cm	200 cm	100 cm	50 cm
0°	0 km	265.5	223.1	171.1	144.7
0°	4 km	192.0	174.1	154.0	144.7
0°	12 km	193.9	158.5	146.2	144.7
45°	0 km	338.1	295.0	248.0	224.1
45°	4 km	276.1	251.0	231.7	224.1
45°	12 km	280.1	242.4	228.1	224.1

Table 34: Generalized fitting error as a function of interactuator pitch and zenith angle for a 3 DM system. The interactuator pitch is changed one DM at a time.

6 Wavefront error budget

A wavefront error budget is developed for the case of an observation at zenith. Where the error term is wavelength dependent, the results for H-band are used.

6.1 High-order wavefront errors

An error budget corresponding for the simulations using Configuration 3 is tabulated in Table 35.

Error term	Cause	Value
Atmospheric bandwidth	Frame rate	50 nm
Measurement noise	Photon return and noise	43 nm
Tomographic reconstruction	Number, location and altitude of WFSs	170 nm
Generalized fitting	Number of DMs	204 nm
Tip-tilt atmospheric bandwidth		25 nm
Tip-tilt noise		0 nm
Tip-tilt tomography		126 nm
Scintillation	High-altitude turbulence	18 nm
Dome seeing		39 nm
LGS focus	Sodium height variations	30 nm
High-order telescope bandwidth	Vibrations	
M2 print-through	Secondary mirror	147 nm

Table 35: Wavefront error budget for the major high-order terms and the lowest possible tip-tilt terms corresponding to the simulations presented in Section 13 (shaded in gray). The red shading represents items not included in the simulations.

The reduction in Strehl due to scintillation from uncorrected turbulence for the median turbulence profile at zenith is 0.64%, 0.47% and 0.33% at J-, H- and K-bands respectively. The effect of scintillation will decrease if the order of the DMs mirrors the order of the atmospheric turbulence (from lowest to highest altitudes), and increase if the DM order is reversed. Since the effect is small, we will ignore scintillation in this study.

6.2 Tip-tilt errors

In this section, we consider the wavefront errors due to the limitations in tip-tilt correction. This includes global tip-tilt as well as field-dependent tip-tilt errors.

For a circular telescope, the conversion between an angle-of-arrival (AA) error in (arcseconds) in one axis and the RMS wavefront error is:

$$\sigma_{wf} = \frac{AA}{206265} \frac{D}{4} \quad (4)$$

Setting $D=7.9$, this gives 9.57 microns for a 1 arcsecond tip or tilt. For a telescope with a diameter of 7.9 m and a circular obscuration of 1.3 m, we find numerically that 1 arcsecond of tilt corresponds to 9.74 microns of wavefront.

Error term	Cause	Best	Typical
Bandwidth	Frame rate	234 nm	
Measurement noise	Photon return and noise	0 nm	
Tomographic error 1 NGS	NGS location	254 nm	303 nm
Tomographic error 2 NGS	NGS location	178 nm	236 nm
Tomographic error 3 NGS	NGS location	125 nm	172 nm
Tomographic error 4 NGS	NGS location	95 nm	
Tomographic error 6 NGS	NGS location	52 nm	

Table 36: Tip-tilt error budget for bright tip-tilt stars

For each number of stars in the field (1, 2 or 3), the best asterism was found by optimizing the radius of a symmetrical constellation. The typical asterism was obtained using a Monte-Carlo simulation assuming that the stars are evenly distributed in the field. The asterisms used are recorded in Table 37.

NGS	Best (arcsec)	Typical (arcsec)
1	[0,0]	[40,0]
2	[-34,0] [34,0]	[-35,-2] [-20,38]
3	[0,38] [-33,-19] [33,-19]	[19,3] [48,15] [-32,-46]

Table 37: Asterisms used to calculate the tip-tilt tomography error

The asterism used in the simulations in Section 13 has a tip-tilt tomographic error of 126 nm, which is very close to the optimal value of 125 nm.

For fields with a lot of stars, the tip-tilt tomographic error can be reduced by adding more stars. A four star constellation can have a tomographic error as low as 95 nm, with a corresponding number

of 52 nm for a six star constellation.

6.3 Focus errors

We consider the focus errors due to sodium height variability. The data used in this analysis comes from the University of British Columbia's lidar system in support of the TMT AO system.²²⁻²³ The data captures the sodium layer profile with 20 ms temporal sampling and 3.6 m vertical sampling. An example of one night's profile is shown in Figure 38.

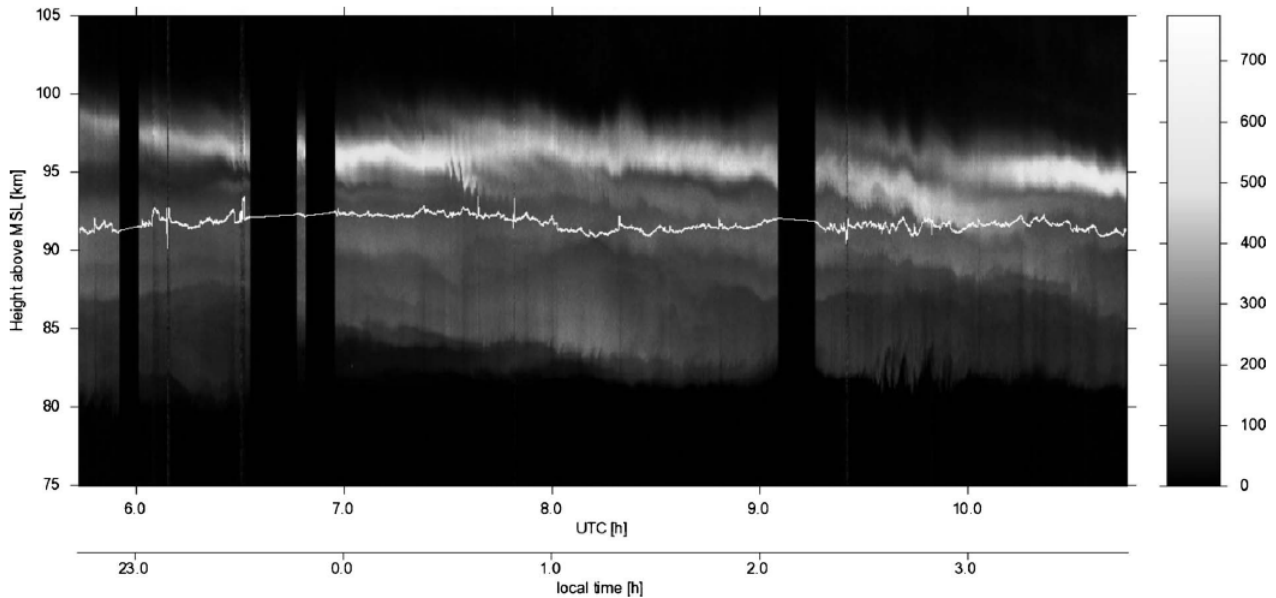


Figure 38: Sodium density evolution as a function of altitude and time. The squiggly line represents the centroid of the altitude. The four gaps in the data are due to automatic shutdowns due to aircraft.²²

The mean altitude is 91 km, with a FWHM of 12 km.²² It is interesting to note that the sodium is not found outside of the altitude interval between 80 and 100 km above sea level. This is because sodium ionized above 100 km and reacts chemically with oxygen below 80 km.

Figure 39 shows the temporal power spectrum of the sodium mean altitude. The power spectrum can be well described as a power law with a slope index taking values in the range -1.95 ± 0.12 , while the amplitude is typically $30 \pm 20 \text{ m}^2/\text{Hz}$. We use this power law to calculate the bandwidth requirements.

²²T. Pfrommer and P. Hickson, "High-resolution lidar observations of mesospheric sodium and implications for adaptive optics," *J. Opt. Soc. Am. A* 27, A97-A105 (2010).

²³Thomas Pfrommer, Paul Hickson, and Chiao-Yao She, "A large-aperture sodium fluorescence lidar with very high resolution for mesopause dynamics and adaptive optics studies", *GEOPHYSICAL RESEARCH LETTERS* 36, L15831 (2009).

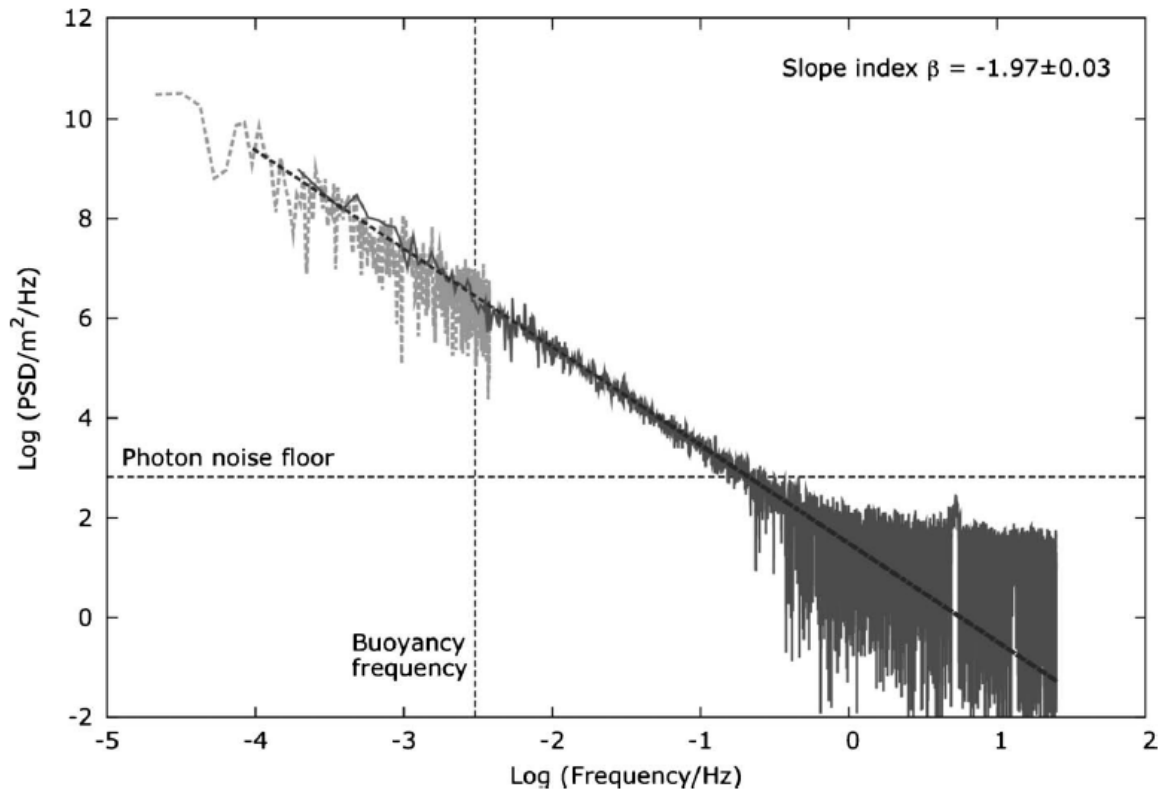


Figure 39: Temporal power spectrum of the sodium mean altitude.²²

The relationship between the change, Δh , in mean sodium altitude, h , and RMS wavefront error, σ , for a telescope with diameter D is given by:²²⁻²³

$$\sigma = \frac{1}{16\sqrt{3}} \left(\frac{D}{h}\right)^2 \Delta h \quad (5)$$

For a 7.9-m telescope, this implies that a 100-m error in sodium altitude estimation leads to 28 nm of wavefront error, and this is the level of accuracy that is required.

We now consider a closed-loop system that is measuring and correcting these focus fluctuations. A simple integral controller with a loop gain of 0.6 and a one frame compute delay is used. The wavefront error as a function of exposure time is plotted in Figure 40. To keep the error to about 30 nm, we need to keep the exposure time around 10 s.

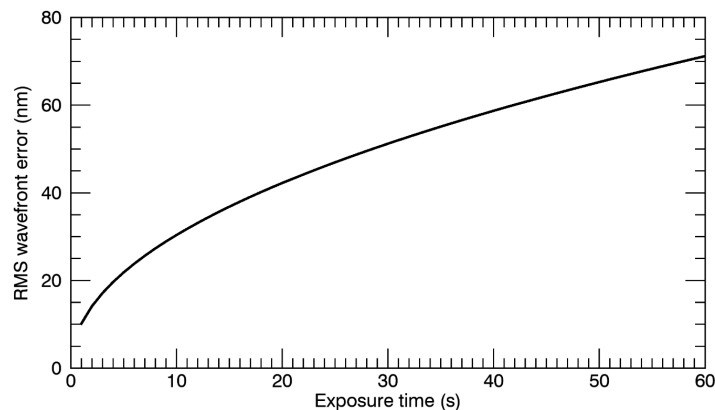


Figure 40: RMS wavefront error due to incorrect sodium height conjugation as a function of exposure time of the slow focus sensor.

7 Conclusions

8 Appendix

In this highly mathematical section, we describe the tomographic reconstructors used in the simulations. These reconstructors are hand-coded in yorick and evaluated before running the simulations.

8.1 LGS tomography

The LGS tomographic reconstructors are based on the original work by Ellerbroek et al.²⁴ These reconstructors have two steps: a tomography step, where the measurements from the 4-6 LGS WFSs are converted into a 3D wavefront estimate at the same resolution as the WFSs using a minimum-variance reconstructor, and a fitting step, which converts the 3D wavefront estimate into DM commands that minimize the wavefront error in the direction of the science targets. In this study, the wavefront was estimated at four altitudes: 0 km, 4 km, 8 km, and 16 km. Future work should investigate whether finer vertical and horizontal sampling, or adjusting the DM altitudes can improve the performance. In addition, the code could be rewritten to reduce the time it takes to compute the reconstructors.

8.2 NGS tomography

In this section, we describe how the tip-tilt tomography is performed. This approach is also documented in a very recent paper by van Dam et al.²⁵

Without loss of generality, let us consider the the least-squares estimate of the on-axis tip-tilt, $\hat{\mathbf{a}} = [\hat{\mathbf{a}}_x, \hat{\mathbf{a}}_y]$, given one or more tip-tilt measurements is given by:

$$\hat{\mathbf{a}} = \mathbf{C}_{as} \mathbf{C}_{ss}^{-1} \mathbf{s} = \mathbf{M} \mathbf{s}$$

where $\mathbf{s} = [[\mathbf{s}_{1x}, \mathbf{s}_{1y}], [\mathbf{s}_{2x}, \mathbf{s}_{2y}], \dots, [\mathbf{s}_{Nx}, \mathbf{s}_{Ny}]]$ are the x and y tip-tilt measurements for stars 1, 2, ..., N .^{26,27} Matrix \mathbf{M} is the reconstructor matrix, which relates how the $2N$ measurements relate to the tip-tilt estimate. The covariance matrices are calculated using the C_n^{-2} profile, the outer scale of turbulence and the telescope diameter, D (the calculations that follow assume a circular telescope with no central obscuration).

In the noiseless case, the angular covariance matrix between two Zernike coefficients, $\mathbf{a}_i(\boldsymbol{\theta}_1)$ and $\mathbf{a}_j(\boldsymbol{\theta}_2)$ of two wavefronts from two sources at directions $\boldsymbol{\theta}_1$ and $\boldsymbol{\theta}_2$ is $\langle \mathbf{a}_i(\boldsymbol{\theta}_1) \mathbf{a}_j(\boldsymbol{\theta}_2) \rangle$. This can be evaluated using the very complicated expression first derived by Whiteley²⁸ and found in Conan.²⁷

In this report, we use a direct calculation of the covariance matrices using numerical integration. The integrand is based on the filter function theory developed by Sasiela.²⁹ The numerical integration is carried out using the *qromo* routine in IDL. The results were found to be identical to

²⁴Ellerbroek, Brent L. "Efficient computation of minimum-variance wave-front reconstructors with sparse matrix techniques." JOSA A 19.9 (2002): 1803-1816.

²⁵Van Dam, Marcos A. et al, "Infrared tip-tilt sensing: on-sky experience, lessons learned and unsolved problems," AO4ELT6 (2019).

²⁶D.T. Gavel, "NGAO real-time controller algorithms design document," v1.1a, (2009).

²⁷R. Conan, "GMT LTAO – Tip-tilt tomography," V1.1 (2010)

²⁸M.R. Whiteley et al, "Temporal properties of the Zernike expansion coefficients of turbulence-induced phase aberrations for aperture and source motion," J. Opt. Soc. Am. A 15 (1998).

²⁹R. Sasiela, "Electromagnetic wave propagation in turbulence," 2nd edition, SPIE Press (2007)

those obtained using Whiteley's formulation.³⁰

The evaluation makes use of the following relationship. Without loss of generality, we assume that one star is at [0,0]. If the second star is located at [θ ,0], then:

$$\begin{aligned}\langle \mathbf{a}_2(0,0)\mathbf{a}_2(\boldsymbol{\theta}, 0) \rangle &= \langle \mathbf{a}_2(0,0)\mathbf{a}_2(0,0) \rangle - 0.5\langle (\mathbf{a}_2(0,0) - \mathbf{a}_2(\boldsymbol{\theta}, 0))^2 \rangle \\ \langle \mathbf{a}_2(0,0)\mathbf{a}_3(\boldsymbol{\theta}, 0) \rangle &= 0 \\ \langle \mathbf{a}_3(0,0)\mathbf{a}_2(\boldsymbol{\theta}, 0) \rangle &= 0 \\ \langle \mathbf{a}_3(0,0)\mathbf{a}_3(\boldsymbol{\theta}, 0) \rangle &= \langle \mathbf{a}_3(0,0)\mathbf{a}_3(0,0) \rangle - 0.5\langle (\mathbf{a}_3(0,0) - \mathbf{a}_3(\boldsymbol{\theta}, 0))^2 \rangle\end{aligned}$$

The right hand side of the equations have two terms. The first term is the tip (or tilt) variance. The other terms are the parallel and perpendicular contributions to the anisokinetic error:

$$\begin{aligned}\langle (\mathbf{a}_2(0,0) - \mathbf{a}_2(\boldsymbol{\theta}, 0))^2 \rangle &= \int_0^\infty d\mathbf{h} \int_0^\infty d\mathbf{k} 2\pi\mathbf{k} \frac{0.0097\mathbf{C}_n^2(\mathbf{h})}{(\mathbf{k}^2 + 1/L_0^2)^{11/6}} \left(\frac{4\mathbf{J}_2(2\pi\mathbf{R}\mathbf{k})}{2\pi\mathbf{R}\mathbf{k}}\right)^2 [1 + 2\mathbf{J}_1(2\pi\mathbf{k}\boldsymbol{\theta}\mathbf{h}) \\ &\quad - 2\mathbf{J}_0(2\pi\mathbf{k}\boldsymbol{\theta}\mathbf{h})]\end{aligned}$$

and

$$\begin{aligned}\langle (\mathbf{a}_3(0,0) - \mathbf{a}_3(\boldsymbol{\theta}, 0))^2 \rangle &= \int_0^\infty d\mathbf{h} \int_0^\infty d\mathbf{k} 2\pi\mathbf{k} \frac{0.0097\mathbf{C}_n^2(\mathbf{h})}{(\mathbf{k}^2 + 1/L_0^2)^{11/6}} \left(\frac{4\mathbf{J}_2(2\pi\mathbf{R}\mathbf{k})}{2\pi\mathbf{R}\mathbf{k}}\right)^2 [1 - 2\mathbf{J}_1(2\pi\mathbf{k}\boldsymbol{\theta}\mathbf{h})]\end{aligned}$$

For small to modest offsets, the variance of the parallel component is three times the variance of the perpendicular component.

An integral in polar coordinates can be written as

$$\int_0^\infty d\mathbf{k} 2\pi\mathbf{k}$$

The integrands have three components:

$$\begin{aligned}\frac{0.0097\mathbf{C}_n^2(\mathbf{h})}{(\mathbf{k}^2 + 1/L_0^2)^{11/6}} &\text{is the filter function for the von Karman power spectrum.} \\ \left(\frac{4\mathbf{J}_2(2\pi\mathbf{R}\mathbf{k})}{2\pi\mathbf{R}\mathbf{k}}\right)^2 &\text{is the filter function for tip-tilt.}\end{aligned}$$

The third term is the anisoplanatic contribution in the parallel and perpendicular directions to the offset. The variance of the tip-tilt terms is obtained by removing the anisoplanatic filter function:

$$\langle \mathbf{a}_2(0,0)\mathbf{a}_2(0,0) \rangle = \langle \mathbf{a}_3(0,0)\mathbf{a}_3(0,0) \rangle = \frac{1}{2} \int_0^\infty d\mathbf{h} \int_0^\infty d\mathbf{k} 2\pi\mathbf{k} \frac{0.0097\mathbf{C}_n^2(\mathbf{h})}{(\mathbf{k}^2 + 1/L_0^2)^{11/6}} \left(\frac{4\mathbf{J}_2(2\pi\mathbf{R}\mathbf{k})}{2\pi\mathbf{R}\mathbf{k}}\right)^2, \text{ where}$$

the factor of half divides the total tip-tilt power into tip and tilt components. R is the radius of the telescope, and all the other symbols have their usual meaning.

For completeness, we state the total anisokinetic error here, which is merely the sum of the parallel and perpendicular components:

$$\sigma^2 = \int_0^\infty d\mathbf{h} \int_0^\infty d\mathbf{k} 2\pi\mathbf{k} \frac{0.0097\mathbf{C}_n^2(\mathbf{h})}{(\mathbf{k}^2 + 1/L_0^2)^{11/6}} \left(\frac{4\mathbf{J}_2(2\pi\mathbf{R}\mathbf{k})}{2\pi\mathbf{R}\mathbf{k}}\right)^2 [2 - 2\mathbf{J}_0(2\pi\mathbf{k}\boldsymbol{\theta}\mathbf{h})]$$

To calculate the covariance when the star offsets are not aligned with either the tip or tilt offsets requires the coordinates to be transformed.

³⁰R. Conan, personal communication (15 March 2011).

Once we have computed these covariance matrices, it is straight-forward to compute the tomographic error:

$\sigma^2 = \text{trace}(\mathbf{C}_{aa} - \mathbf{C}_{as}\mathbf{C}_{ss}^{-1}\mathbf{C}_{as}^T)$, or, in the case of noisy measurements with noise covariance matrix, \mathbf{C}_{nn} :

$$\sigma^2 = \text{trace}[\mathbf{C}_{aa} - \mathbf{C}_{as}(\mathbf{C}_{ss} + \mathbf{C}_{nn})^{-1}\mathbf{C}_{as}^T].$$

This method is extended to calculate the tomographic tip-tilt error over a discrete number of points in the image plane. The tip-tilt command is the tip-tilt value that minimizes the error over the whole science field. The correction of the tip-tilt anisoplanatism modes should also use this approach, but currently does not. Instead, focus and astigmatism are added to the high-altitude DM (the so-called plate scale modes), with the reconstructor consisting of a least-squares inversion of the interaction matrix between the plate scale modes and the tip-tilt measurements on the NGS WFS.

8.3 Performance of 2 laser, 5 LGS system

Following the Conceptual Design Review, it was clear that a system with 5 LGSs similar to Configuration 1 is required. To save money, we would like to use 2 LGSs instead of 3 LGSs. Here, we propagate two off-axis LGSs using light from a single laser, and two off-axis LGSs plus an on-axis LGS using a second laser.

The performance of this configuration was compared with Configurations 1 and 3 as a function of sodium return. The maximum expected sodium return when pointed at zenith is 104 photons/cm²/s per Watt of laser power, while a more typical value used in previous simulations 38.5. Note that the return also reduces with zenith angle. In no case were the reconstructor, control law or frame rate adjusted to account for the change in sodium return. Simulation results presented in Table 20 show that a 2 laser 5 LGS system outperforms a 2 laser 4 LGS system for all sodium returns.

Sodium return	104	52	26	13	6.5
Config 1	0.592±0.066	0.589±0.066	0.584±0.066	0.575±0.066	0.556±0.065
Config 3	0.566±0.065	0.564±0.065	0.559±0.063	0.550±0.062	0.530±0.061
2 laser 5 LGS	0.590±0.066	0.586±0.066	0.579±0.065	0.567±0.063	0.540±0.062

Table 38: K-band Strehl ratio (average and standard deviation across the field) as a function of sodium return for the three different configurations.